The Fabrication and Characterization of a Superconducting Birdcage Resonator

by

Shahab Akmal

A thesis
presented to the University of Waterloo
in fulfillment of the
thesis requirement for the degree of
Master of Applied Science
in
Electrical Engineering

Waterloo, Ontario, Canada, 2018

I hereby declare that I am the sole author of this thesis. This is a true copy of the thesis, including any required final revisions, as accepted by my examiners.

I understand that my thesis may be made electronically available to the public.

Abstract

In this thesis we presents the fabrication and characterization of a superconducting Birdcage style radiofrequency (RF) coil, a commonly used coil design in nuclear magnetic resonance (NMR) spectrometers. The Birdcage was fabricated from a series of superconducting Niobium thin film resonators, deposited onto sapphire wafer by sputtering deposition. The resonators were assembled into the 3 dimensional birdcage coil, and housed in a custom machined RF package. The fabrication, assembly tools, and procedures are presented. A numerical model, based on lumped-element eigenanalysis, was used to describe the resonance structure of the coil. We show that misalignment in the assembly can lead to an increase in the resonant frequency of the transverse mode when compared to the analytical description. A set of low temperature measurements were performed to characterize the quality factor, magnetic field, and power dependence. A modest improvement in the Q, over non-superconducting Birdcage coil, is shown. Simulations, in HFSS, of the field and current distribution, as well as changes in the quality factor from experimental measurements of the coil are presented. The coil was perturbed with an aluminum ball bearing and aluminum sheet in order to demonstrate the existence circularly polarized magnetic field within the Birdcage coil.

Acknowledgements

Foremost, I would like to express my sincere gratitude to my supervisor Prof. David Cory for his continuous support of my Master's research, for his immense knowledge, motivation and patience. With his guidance, I was able to pursue new trains of thought, and discover new areas of research .

Besides my supervisor, i would like to thank my fellow lab members: Dr. Hamid Mohebbi, Dr. Deler Langenberg, Dr. Troy Borneman, Don Carkner, Peter Sprenger, and Alex Mitrovic for their stimulating discussion, tireless devotion to the development and safety of each and every student, and for all the fun times we have had over the years.

Last but not least, I would like to thank my family for their endless support and direction throughout my life.

Dedication

This thesis is dedicated to my family for their constant support, encouragement, and whose example has taught me the value of hard work.

Table of Contents

List of Tables **ix**

List of Figures **x**

1 Introduction **1**

1.1 Nuclear Magnetic Resonance 1

1.1.1 Signal Generation and Detection 3

1.1.2 Radiofrequency Coils 4

1.1.2.1 Birdcage Volume Coil 4

1.2 Outline 6

2 Background **8**

2.1 Lumped-Element Model of Resonator 8

2.1.1 Lumped Element Circuit 8

2.1.2 Quality Factor 10

2.2 Superconductivity 10

2.2.1 Complex Conductivity 11

2.2.2 Surface Impedance 12

2.2.3 Nonlinear Response 13

3 Resonator Fabrication and Experimental Methods **15**

3.1 Birdcage Resonator Fabrication 15
3.1.1 Photolithography 17
3.1.2 Dicing 20
3.1.3 Resonator Assembly 21
3.2 Experimental Setup 21
3.2.1 Vector Network Analyzer 21
3.2.2 Resonator Package 23
3.2.3 Low Temperature Probe 24
3.2.4 Liquid Helium Dewar 25
3.3 Experimental Procedure 25

4 Experiments and Results **27**

4.1 Circuit Analysis of Birdcage Resonator 27
4.1.1 Lumped Element Eigenanalysis 27
4.1.1.1 Perturbation 29
4.2 Experimental Results 31
4.2.1 Empty Birdcage Resonator 31
4.2.1.1 Simulated Field Distribution 31
4.2.1.2 Quality Factor 32
4.2.1.3 Power Dependence 34
4.2.1.4 Magnetic Field Dependence 36
4.2.2 Aluminum Ball Bearing 37
4.2.2.1 Quality Factor 37
4.2.2.2 Simulated Current Distribution 38
4.2.3 Aluminum Sheet 41

4.2.3.1 Quality Factor 41

4.2.3.2 Simulated Current Distribution 42

5 Conclusion **46**

5.1 Conclusion 46

List of Tables

3.1 The properties, and associated values, of the CrysTec sapphire wafer used for fabrication. 15

4.1 Measured value of Q, resonant frequency f_0, and microwave loss at variable separation of the feed-line loops to the resonator. 33

4.2 Measured values of Q, resonant frequency f_0, and loss at varied input microwave power P_{in}. 35

4.3 Measured values of Q, resonant frequency, and loss of the empty resonator, with the addition of the g10 rod, and the combination of the g10 rod and ball bearing. 38

4.4 Measured values of Q, resonant frequency f_0, and loss of the resonator with the addition of an aluminum sheet in multiple orientations. 42

List of Figures

1.1 Zeeman splitting of a spin-$\frac{1}{2}$ particle [1]. 2

1.2 The layout of the phase sensitive detector, shown in (a), used for signal demodulation of a high-frequency signal precessing at the Larmor frequency. Two orthogonal PSDs, shown in (b), is used for quadrature detection. [1] 4

1.3 The design of the RF birdcage coil, as seen in [2]. The circular loops, depicted as Z_R, are the end-rings of the birdcage. The straight rungs, depicted as Z_L, are the legs of the birdcage. When impedance elements are placed both within the rings and the legs of the coil, the birdcage is in its band-pass configuration. . 5

1.4 Shown here are the three possible configuration of the RF birdcage coil [3]: a) low-pass, b) high pass, and c) band pass. The low-pass configuration has capacitors along the legs of the coil. The high-pass has capacitors along the end-rings, and the band-pass has them distributed along the legs and the end-rings of the coil. 5

2.1 The lumped-element series model of a microwave resonator. A resistor, R, an inductor, L, and a capacitor, C, are placed in series with a voltage source V_s [4]. 9

2.2 The equivalent circuit representation of complex conductivity where the total current is split between an inductor and resistor. The inductor represents the imaginary component of the complex conductivity and the superconducting channel. The resistor represents the real component of the complex conductivity and the normal channel [5]. 12

3.1 Omicron UHV sputtering system used to deposit Niobium films onto the sapphire wafers. 16

3.2 Outline of the process used to fabricated the birdcage resonator a) a blank, 2 inch, 430 microns thick sapphire wafer is cleaned and placed within the sputtering chamber of the omicron UHV system, b) 100 nm of Niobium is deposited on the top surface of the sapphire wafer, c) the wafer is transported to the QNF where a 500 nm thick layer of photoresist is spin coated onto the wafer, d) exposed for 2.7 seconds at a lamp power of 380-420W to imprint the resonator design, e) dry-etch RIE to remove undeveloped resist areas, to reveal f) the final resonator pattern. 18

3.3 The resonator design fabricated on a 430 micron thick sapphire wafer measuring 27mm in length, and 10mm in width. This design is one of two which makeup the birdcage resonator. The second design has a larger width at 10.86mm, illustrated below in figure 3.3. The smaller resonator is intended to fit in between the edge of the wafer and the beginning of the niobium conductor. 19

3.4 An enhanced view of the two resonators. Resonator a) has a width 10.86 mm and b) 10 mm. The wider of the two resonators, (a), has a 430 micron gap at the edge of the wafer in order for resonator (b) to make a seamless connection. The gap between the ring conductors and the center conductor, in both designs, is 100 nm. 20

3.5 The two accessory components used in the assembly of the birdcage resonator. a) NOA81 is a single component, polymer-based, liquid adhesive used to secure the individual resonators together. b) the 90 brass wedge used to align the resonators together. 21

3.6 A top down view of the empty birdcage resonator placed within a custom copper packaging. The resonator measures 27 mm in height, 10.86mm in width, and 10mm in length. The resonator package is 40mm in diameter and 40mm in height. The two feed-line loops, positioned on opposite sides and separated by a 5mm gap to the face of the resonator, are used to couple into the resonator. The loops are made from the inner conductor of the feed-line loops, soldered to its outer shield. The diameter of the loops are 0.36mm and the length is 20mm. The feed-lines are made from RG-405 semi-rigid coaxial cable purchased from Pasternack. 22

3.7 The copper package designed to house the birdcage resonator in the liquid helium dewar. The body of the package, (a) measures 40 mm in height, with an inner diameter of 39mm and outer diameter of 40mm. The wall thickness, as measured at the center of the package, is 1mm. The plate, shown in (b), is 42mm in diameter, including the lip to connect to the body of the package. The inner platform is 39mm in diameter and 2mm in height. 23

3.8 The full CAD model of the birdcage package, along with coaxial feed-line cables, attached to an L-bracket. The L-bracket is used to secure the package to the low temperature probe. The bracket measures 15cm in height, with a thickness of 2mm, and a length of 45mm. The coaxial feed-lines are 20 mm in length, and extend from the body of the package to the coaxial connectors of the probe. 24

3.9 Low temperature probe 24

3.10 The complete experimental setup used to characterize the Birdcage resonator. The two-port VNA is connected to the birdcage resonator via coaxial cables attached to the low temperature probe at the top of the Helium Dewar. . . . 26

4.1 The ladder network representing the birdcage resonator. Each cell is composed of two leg elements Z_L, and two ring elements Z_R. The network is symmetric [6]. 27

4.2 Perturbation of the resonant frequency of the transverse mode. The perturbation parameter δ is varied from 0 to 1. 30

4.3 A side view of the empty birdcage resonator, secured within the copper package, as modeled in HFSS. The birdcage is fixed to the rogers laminate at the base of the package and centered inside the package. The gap between the feed-line loops and resonator legs is initially fixed at 4mm. The cord grips, not shown here, can be adjusted to increase or decrease the gap. 31

4.4 The magnetic field distribution within the empty resonator, as simulated in HFSS. The resonator generates a magnetic field in the direction perpendicular to the feed-line loops. The sample, in the center, is simulated as lossless. The input power is P_{in} = 1 W, and s_{21max} = -0.94dB. The Q of the simulated resonator is 5768 and f_0 = 3.019425 32

4.5 The transmission, S_{21}, measurement of the transverse mode of the empty birdcage resonator. The separation distance is measured from the outside face of the resonator to the feed-line loop. The separation is varied, beginning at 4mm, up to a maximum of 7mm. The quality factor of the resonator is measured using the 3dB method. Higher separation distances is observed to increase the measured Q. 33

4.6 Transmission measurement of the transverse mode taken at difference input microwave powers, from -30dB to -10dB. The power dependent measurement is used to observe the non-linearity of the resonator. At powers greater than -10dB, the shape of the resonant curve is no longer Lorenztian. 34

4.7 Plot of Q vs $\frac{\Delta f_0}{f_0}$ of the empty birdcage resonator. The results show the decrease in quality factor with an increase in relative shift of the frequency at higher microwave power. 35

4.8 The dependence of the quality factor, $Q_{measured}$, on the applied magnetic field strength, B. 36

4.9 Placement of the aluminum ball bearing in the center of the birdcage resonator. The aluminum ball bearing is 3mm in diameter. The center of the ball is aligned to the center of the package and the feed-line loops. 37

4.10 Magnitude of S_{21} of the transverse mode of the empty resonator, the resonator with the dielectric support only, and the resonator with the dielectric support and aluminum ball bearing. The separation of the feed-line loops, to the resonator, is maintained at 6mm. A coupling between the feed-lines is still present as a peak adjacent to the resonance peak, at a lower frequency. 38

4.11 Simulation of the surface current distribution of the birdcage resonator, with the addition of a aluminum ball bearing. The simulation is done using HFSS. The Q of the resonator is 5698, a drop of 100 from the Q of the empty resonator, and the resonance frequency is f_0 = 3.0221GHz, a shift of 0.0027 Ghz. The simulated input power, with the ball bearing, is P_{in} = 1 W, loss is P_{loss} = 0.032W, s_{21max} = -1.13dB. 40

4.12 Placement of the aluminum sheet in two orientations within the resonator, where a) shows the parallel orientation and b) shows the perpendicular orientation. The aluminum sheet is 15mm in length, 5mm in width and 0.3mm in thickness. The center of the sheet is aligned to the center of the package and the feed-line loops. 41

4.13 Magnitude of S_{21} on the transverse mode of the empty resonator, the parallel, and the perpendicular orientation of an aluminum sheet inserted within the resonator. The feed-line separation is maintained at 6mm. The feed-line coupling is still present, as a peak to the right of the resonance peak of the empty resonator. However, with the presence of the aluminum sheet in different orientations, the coupling may be masked by the conductor. 42

4.14 Simulation of the current distribution in the aluminum sheet set in the parallel orientation. The input power, P_{in}, is set to 1W, the simulated loss is P_{loss} = 0.124 W, and the S_{21max} = -3.41dB. The simulated Q is 4377, a large drop in Q compared to the empty resonator, and f_0 = 3.06545, a shift of 0.046025GHz. 43

4.15 Simulation of the surface current distribution with the aluminum sheet in the perpendicular orientation. The input power, P_{in}, is set to 1W, the simulated loss is P_{loss} = 0.094W, and the s_{21max} = -1.524dB. The simulated Q is 5036, a drop in Q of 732, and f_0 = 3.021675, a shift of 0.00225GHz. 45

Chapter 1

Introduction

In chemistry, nuclear magnetic resonance (NMR) has been widely used for the past five decades to investigate the structure and composition of atoms and molecules. The continuous development of its hardware has made NMR an essential tool in spectroscopy. The ability to perform non-invasive measurements has also enriched the filed of medicine, where Magnetic Resonance Imaging (MRI) has become essential in medical examination. However, the low sensitivity of current systems is a limitation in NMR [7].

The development of superconducting microwave resonators as radiofrequency coils for NMR has taken significant steps forward. The use of superconducting materials such as YBCO [8] or Niobium [9, 10, 11, 12, 13, 14], and operating at cryogenic temperatures can effectively optimize the coils beyond their room temperature equivalents. Decreasing the noise in the transducer of the magnetic resonance system, or the sample under investigation, can improve signal-to-noise (SNR).

1.1 Nuclear Magnetic Resonance

To observe NMR, nuclei under investigation must have a non-zero angular moment $\vec{I}$ and magnetic moment $\vec{\mu}$. They are related to each other by $\vec{\mu} = \gamma\vec{I}$, where γ is the gyromagnetic ratio of a nucleus. A strong external magnetic field, $\vec{B_0}$, is applied to initiate a macroscopic magnetism and manipulate $\vec{\mu}$. The external field induces a splitting of the nuclei energy levels, which is measured by NMR. This splitting is known as the Zeeman splitting, and is proportional to the magnetic moment of the nucleus and the strength of the applied magnetic field

$$\Delta E = -\vec{\mu} \cdot \vec{B_0} \tag{1.1}$$

The most commonly used spin system, hydrogen, is a quantum spin-$\frac{1}{2}$ particle ($m_I = \pm\frac{1}{2}$). In the absence of an external magnetic field, the nuclear spin has two degenerate energy eigenstates. These two states are the low and high energy states, or spin-up $|\uparrow\rangle$ and spin-down $|\downarrow\rangle$, separated in energy by

$$\Delta E = E_\downarrow - E_\uparrow = \gamma\hbar\vec{B_0} \tag{1.2}$$

shown in figure 1.1.

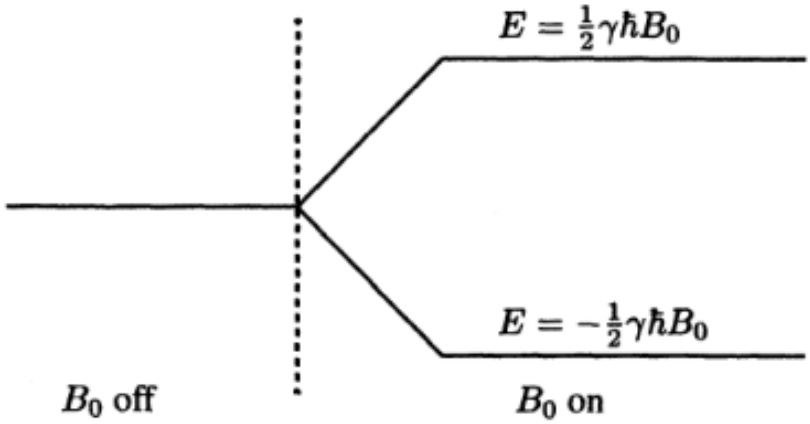

Figure 1.1: *Zeeman splitting of a spin-$\frac{1}{2}$ particle [1].*

Conversely, in the presence of an external magnetic field, the energy eigenstates split into two levels. The magnetic moment will experience a torque as the change in its angular momentum,

$$\frac{d\vec{I}}{dt} = \vec{\mu} \times \vec{B_0} \tag{1.3}$$

This torque, or nuclear precession as it is called, rotates at an angular frequency of ω_0, known as the Larmor frequency.

When considering a physical sample, the NMR signal will measure the combined effect of the magnetic field on all of the atoms present in the sample. The behavior, then, of the entire spin system can be described by a net magnetization vector, $\vec{M}$, which represents the vector sum of all the magnetic moments $\vec{\mu_n}$

$$\vec{M} = \sum_{n=1}^{N_s} \vec{\mu_n} \tag{1.4}$$

where N_s is the total number of spins in the system. The net magnetization is broken up into its component along the static magnetic field, or longitudinal magnetization M_z, and the transverse magnetization's M_x and M_y, which are perpendicular to $\vec{B_0}$. At equilibrium, the transverses magnetization are zero, and only a small net longitudinal magnetization exits.

1.1.1 Signal Generation and Detection

In a physical sample, the static magnetic field alone is not enough to generate an NMR signal as the individual spins are not in phase. The application of an short-lived RF pulse $\vec{B_1}(t)$, oscillating at the Larmor frequency of the spins, is used to tip the magnetization $\vec{M}$ into the transverse plane. The spin system is then no longer in thermal equilibrium and, only when the RF pulse is removed, will it return to it. This restoration is reflected by two time constants: T_1, and T_2. T_1 represents the recovery of thermal equilibrium, established by the static magnetic field, and is called the spin-lattice relaxation time. T_2 represents the loss of the phase coherence established by the RF pulse, and is called the spin-spin relaxation time. During this decay process the magnetization $\vec{M}$ will precess about $\vec{B_0}$, known as the free precession. The NMR coil is designed to measure this precessing transverse magnetization as an induced voltage across the resonant coil. The time-varying magnetic flux through the resonant coil generates a voltage equal to the rate of change of magnetic flux in the coil. By placing the coil in close proximity to the precessing magnetization, it can be used to detect an electromotive force (EMF).

The magnetic flux through the coil is given by

$$\phi(t) = \int_{spin\ ensemble} \vec{\boldsymbol{B}}_{\boldsymbol{r}}(\boldsymbol{r}) \cdot \vec{\boldsymbol{M}}(\boldsymbol{r}, t)\, dr \tag{1.5}$$

The voltage induced in the coil can be found using Faraday's law

$$V(t) = -\frac{\partial \phi(t)}{\partial t} = -\frac{\partial}{\partial t} \int_{spin\ ensemble} \frac{\vec{\boldsymbol{B}}_{\boldsymbol{r}}(\boldsymbol{r}) \cdot \vec{\boldsymbol{M}}(\boldsymbol{r}, t)\, dr}{|\boldsymbol{B}_{\boldsymbol{r}}|} \tag{1.6}$$

where $V(t)$ is the raw NMR signal, and this equation allows us to quantify the magnetic resonance signal [1].

However, the induced voltage is a high-frequency signal precessing at the Larmor frequency and must be demodulated to a lower frequency. The signal demodulation is done using the quadrature detection scheme where two orthogonal phase-sensitive detectors (PSD) are used to remove the high-frequency component. A single PSD accomplishes the signal

frequency conversion by first comparing it to a reference sinusoidal signal and then low-pass filtering the signal to remove the high-frequency component. The detection scheme is shown in figure 1.2.

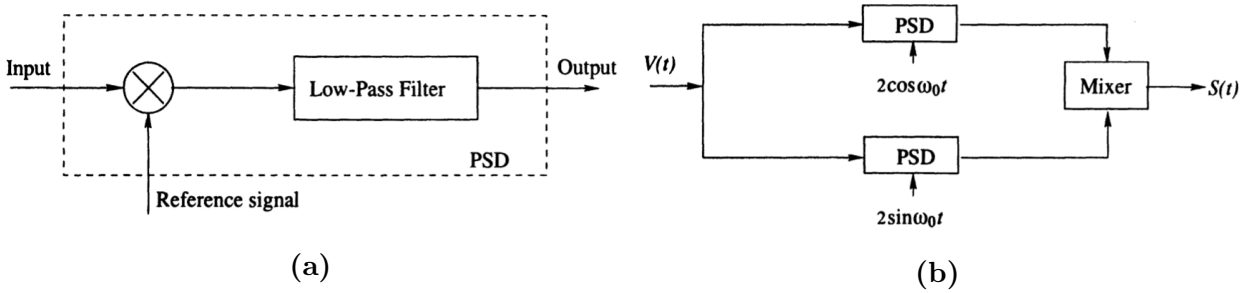

Figure 1.2: *The layout of the phase sensitive detector, shown in (a), used for signal demodulation of a high-frequency signal precessing at the Larmor frequency. Two orthogonal PSDs, shown in (b), is used for quadrature detection. [1]*

1.1.2 Radiofrequency Coils

The radio frequency (RF) coil is the transducer through which the nuclear spins are excited, manipulated, and measured. The design of the RF coil has a large influence on the SNR, and hence the overall performance, of the NMR spectroscopy. Ideally, the coil chosen is capable of providing both a highly uniform B_1 field with a high SNR in order to achieve a high-sensitivity spectrum.

Two types of RF coil are commonly used in NMR: the volume, or surface coils. The volume coil has the ability to maintain excellent field homogeneity and operate in quadrature, in comparison to the surface coil. Operating in quadrature allows a volume coil to generate a circularly polarized field, as supposed to a linear polarized field of simple coils. The most popular type of volume coil is the birdcage coil. The birdcage coil is the focus of this thesis and is discussed in more detail in the following section.

1.1.2.1 Birdcage Volume Coil

The RF birdcage coil was first proposed in the early 1980s [15], and is capable of producing highly homogeneous magnetic fields over its volume. The design has been under continuous developed, fine tuned to increase sensitivity and field homogeneity to provide high SNR. The birdcage coil has the added benefit of operating in quadrature, which over linear excitation, provides up to $\sqrt{2}$ increase in the power efficiency and magnetic resonance signal

sensitivity [16].

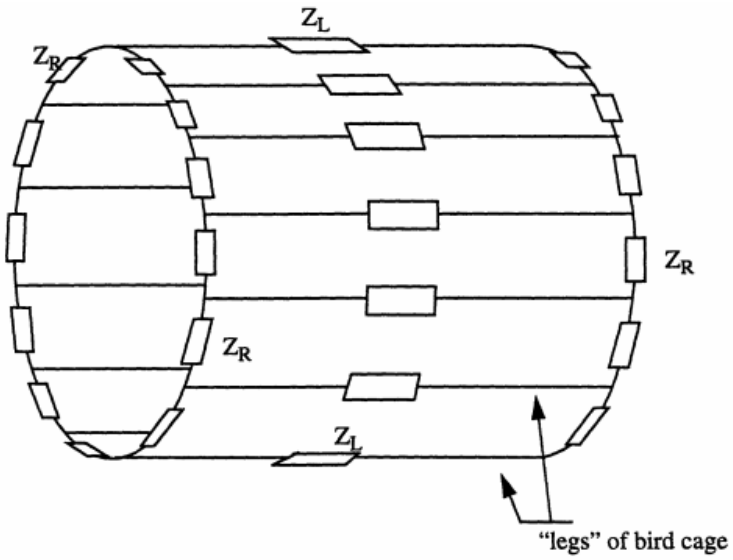

Figure 1.3: *The design of the RF birdcage coil, as seen in [2]. The circular loops, depicted as Z_R, are the end-rings of the birdcage. The straight rungs, depicted as Z_L, are the legs of the birdcage. When impedance elements are placed both within the rings and the legs of the coil, the birdcage is in its band-pass configuration.*

The design of the birdcage coils is typically is a cylindrical geometry where two circular loops at either end of the coil, referred to as rings, are held together by a series of straight rungs, or legs. An example birdcage coil is show in figure 1.3. For application in magnetic resonance, the placement of the capacitors in the coil geometry results in three important configurations: low-pass, high-pass, and the band-pass coil. The low-pass coil is a result of placing capacitors along the legs, shown in figure 1.4a. The high-pass coil has capacitors distributed along the end-rings, and the band-pass coil has them both in the legs and the end-rings, shown in figure 1.4b and figure 1.4c respectively.

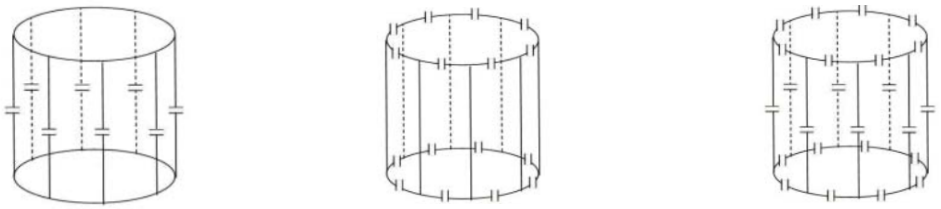

Figure 1.4: *Shown here are the three possible configuration of the RF birdcage coil [3]: a) low-pass, b) high pass, and c) band pass. The low-pass configuration has capacitors along the legs of the coil. The high-pass has capacitors along the end-rings, and the band-pass has them distributed along the legs and the end-rings of the coil.*

As a transmitter, the sinusoidal driving current is distributed along the legs of the birdcage in success $\frac{2\pi}{N}$ phase shifts, where N is the number of legs. This distribution is necessary

to produce a uniform circularly polarized magnetic field within the birdcage volume. The vector sum of the induced magnetic field is a perpendicular to the static magnetic field of the form

$$\vec{\boldsymbol{B}}_{\mathbf{1}} = B_1[cost(\omega t)\hat{x} + sin(\omega t)\hat{y}] \tag{1.7}$$

The phases difference created by the distribution of capacitors along the coil, along with the sample centered within the birdcage, are excited by a driving current oscillating at the Larmor frequency of the sample. The current at the n^{th} run can be written as

$$\boldsymbol{I_n} = I_0 sin(\omega t + \phi) \tag{1.8}$$

where I_0 is the driving current.

As the receiving chain, the birdcage coil is designed to operate in quadrature. It can simultaneously detect a transverse field along two orthogonal directions. The signal can be recombined with the appropriate electronic circuit, external to the resonator, to generate a resonant spectrum.

The birdcage coil can be modeled using lumped circuit analysis, and the basic modes of operation and corresponding resonance frequencies can be calculated using mesh analysis [6, 17, 18]. This analysis is done in chapter 2. However, it is valid only at low frequencies. In order to predict the performance at higher frequencies, full-wave simulation software such as ANSYS's HFSS can be used to develop a full electromagnetic profile of the resonator and solve the necessary time-dependent Maxwell equations.

1.2 Outline

The aim of this thesis is to experimentally study a superconducting birdcage resonator as a RF probe in NMR spectroscopy. The use of superconducting materials is based on improving the SNR ratio which may limit the performance of high-sensitivity NMR. The development of the RF coil performance is critical in achieving this. Optimization with respect to the coil geometry, uniformity of the magnetic field over the sample, and the quality factor is needed. These parameters are dependent on the design requirements of the coil and the sample under investigation.

The birdcage resonator is introduced and a brief introduction to NMR theory required for interpreting the results of this thesis. In chapter 2, the theory of microwave resonators and superconductivity are briefly introduced. In chapter 3 the experimental setup is discussed.

In chapter 4, the results of a series of experiments to characterize the resonator are given. Finally, in chapter 5, conclusions are presented, and a discussion of future work is given.

Chapter 2

Background

2.1 Lumped-Element Model of Resonator

The simplest electrical model of the microwave resonator is that of the lumped-element resonators presented in circuit theory. We can model it as either a series or a parallel RLC circuit, when excited at frequencies near its resonance.

2.1.1 Lumped Element Circuit

The basic model is that of the resonant circuit, shown in figure 2.1, with resistive, inductive, and capacitive elements either in series or parallel [4]. The input impedance of the series circuit is

$$Z_{in} = R + j\omega L - j\frac{1}{\omega C} \tag{2.1}$$

where C is a capacitor, R is a resistor, L is an inductor, and ω is the angular frequency. The complex power, P_{in}, delivered to the resonator by a sinusoidal voltage sources, V_s, is

$$P_{in} = \frac{1}{2}|I|^2(R + j\omega L - j\frac{1}{\omega C}) \tag{2.2}$$

The time-average energies stored in the capacitor and the inductor are

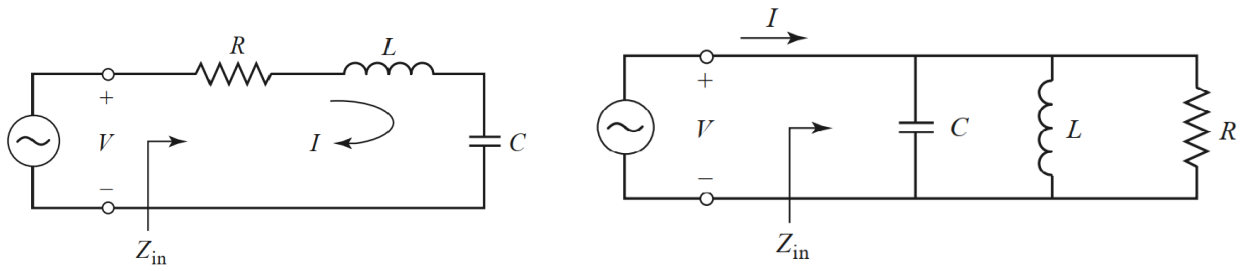

Figure 2.1: *The lumped-element series model of a microwave resonator. A resistor, R, an inductor, L, and a capacitor, C, are placed in series with a voltage source V_s [4].*

$$W_e = \frac{1}{4}|V|^2 C \tag{2.3a}$$

$$W_m = \frac{1}{4}|I_L|^2 L \tag{2.3b}$$

where I_L is the current through the inductor, W_e is the stored electrical energy, and W_m is the stored magnetic energy. The total energy $W = W_m + W_e$. When the input impedance is written in terms of 2.3a and 2.3b, we note it becomes real when $W_e = W_m$ and the circuit is at resonance. The resonance frequency is

$$\omega_0 = \frac{1}{\sqrt{LC}} \tag{2.4}$$

In addition, when discussing resonant circuit, the quality factor Q is an important characteristic. The quality factor, Q, is broadly defined as

$$Q = \omega \frac{W_m + W_e}{P_{loss}} \tag{2.5}$$

where the loss is the power dissipated by the resonator is

$$P_{loss} = \frac{1}{2}|I|^2 R \tag{2.6}$$

Thus, the quality factor describes the energy loss of a resonant circuit. Sources of loss such as conductor loss, dielectric loss, or radiation loss of the material or external circuit will reduce the Q of the resonant circuit. For a series circuit, the unloaded, or internal, quality factor Q_i of the series resonant circuit is

$$Q_i = \frac{1}{\omega_0 RC} = \frac{\omega_0 L}{R} \tag{2.7}$$

At frequencies near resonance, we can approximate the input impedance as

$$Z_{in} = \frac{R}{1 + j2L(\omega - \omega_0)} \tag{2.8}$$

A similar derivation for parallel resonance circuits results in an input impedance of

$$Z_{in} = \frac{R}{1 + 2jQ_i\frac{(\omega-\omega_0)}{\omega_0}} \tag{2.9}$$

2.1.2 Quality Factor

As discussed above, the measured quality factor of a resonator is a combination of the internal sources of loss such a dielectric loss, and external loss, which depends on the coupling to external circuitry. The overall quality factor, or loaded quality factor Q_L, is then

$$\frac{1}{Q_L} = \frac{1}{Q_i} + \frac{1}{Q_e} \tag{2.10}$$

where Q_i is the internal and Q_e is the external quality factor.

2.2 Superconductivity

Superconductors are characterized by two properties: perfect conductivity ($\rho = 0$), and perfect diamagnetism. Although, perfect conductors differ from superconductors based on the interaction of the conductor with a magnetic field. In superconductors, this interaction is explained by the Meissener effect. If placed in a magnetic field, a perfect conductor will develop a surface current which opposes, and cancels, the external field to a thin layer near the surface. The difference is that in superconductors, the magnetic field is expelled from the interior of the material. The infiltration of an external field, which decays exponentially into the material, is defined as the London penetration depth, λ.

Superconductivity can be understood by examining the microscopic process of electron transport within a material. While electrons in normal metals travel independently of each other; in a superconductor, electrons are grouped into Copper pairs. The distance at which

the electrons are correlated is defined as the coherence length ξ. The motion of these paired electrons is without resistive loss, and is one of the main qualities of a superconductor.

There exists two types of superconductors: Type-I, and Type-II superconductors. Type-I superconductor are where the coherence length is greater than the penetration depth. The complete expulsion of magnetic flux endures for magnetic field less than the critical magnetic field, H_c, and a characteristic of the material. Above the critical field, superconductivity is destroyed. Type-II superconductors are where the coherence length is equal to or less than the penetration depth. Materials of this nature exclude magnetic fields up to a lower critical field, H_{c1}. After which magnetic fields are able to penetrate, but it remains in a superconducting state until its upper critical field, H_{c2}. A type-II material in between the lower and upper critical fields, is said to exist in a mixed state.

2.2.1 Complex Conductivity

At finite temperatures, the density of superconducting electrons is proportional to the density of normal electrons and approximately

$$n_s = n_n(1 - (\frac{T}{T_C})^4) \tag{2.11}$$

where $\frac{T}{T_C}$ is known as the reduced temperature. At temperatures much less than T_C, most carriers exists as Copper pairs, but as it approach T_C the fraction of Copper pairs will approach zero. When exposed to a time dependent electric field, the total current density is

$$J = J_n + J_s = \sigma_{TF}E \tag{2.12}$$

where σ_{TF} is the two-fluid model of conductivity, otherwise known as the complex conductivity. It consists of a real component, σ_1, which represents normal electrons, and an imaginary component, σ_2, which represents the Copper pairs. The total current density is

$$J = (\sigma_1 - j\sigma_2)E \tag{2.13}$$

where σ_1 and σ_2 are

$$\sigma_1 = \frac{n_n e^2 \tau}{m(1 + \omega^2\tau^2)} \tag{2.14a}$$

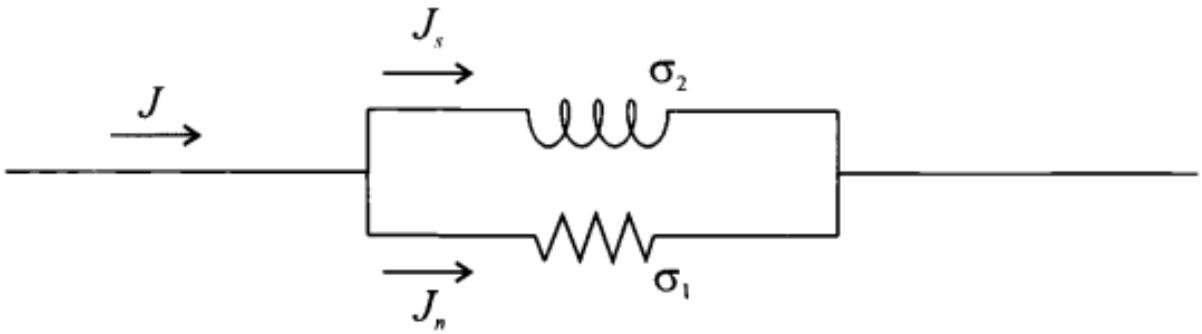

Figure 2.2: *The equivalent circuit representation of complex conductivity where the total current is split between an inductor and resistor. The inductor represents the imaginary component of the complex conductivity and the superconducting channel. The resistor represents the real component of the complex conductivity and the normal channel [5].*

$$\sigma_2 = \frac{n_s e^2}{\omega m} + \frac{\omega n_n e^2 \tau^2}{m(1+\omega^2\tau^2)} \tag{2.14b}$$

and where τ_n is the relaxation time of a normal electron, ω is the frequency of the AC signal in the superconductor. In practice, $(\omega\tau)^2 \ll 1$.

The concept of complex conductivity is also described by a simple equivalent circuit shown in figure 2.2. The total current density, J, is considered to be split between the superconducting channel, modeled as a reactive inductance, and a normal channel, modeled as a resistor. For a DC current, the inductor acts as a short and allowed the current to move through it without resistance. For an AC signal, at low frequencies, more current flows through the inductor due to a lower reactance of the circuit. At higher frequencies, the inductor begins to act more like an open circuit, and the current begins to flow through the resistor. This analogy accounts for the critical current density property of superconducting film, and the destruction of superconductivity at high frequency AC signals.

2.2.2 Surface Impedance

The surface impedance is defined as the ratio of the electric field to surface current,

$$Z_s = \frac{E_t}{J_s} = R_s + iX_s \tag{2.15}$$

It is an important feature for determining the RF properties of a material. For a purely resistive material,

$$R_s = \sqrt{\frac{\mu_0 \omega}{2\sigma}} = \mu_0 \omega \delta_c \tag{2.16}$$

where δ_c is the classical skin depth which quantifies the depth of penetration of a magnetic field into a metal, and σ is the DC conductivity. The propagation constant, γ, is

$$\gamma = \alpha + j\beta = \sqrt{(j\omega\mu(\sigma + j\omega\epsilon))} \tag{2.17}$$

where α is the attenuation constant, and β is the phase of the propagating wave.

For a material with kinetic inductance, the electron mean free path, l, is larger than δ_c, and Ohm's law is no longer valid. This results in the theory of anomalous skin effect [19]. The propagation constant and the surface impedance can be found by introducing the complex conductivity, $\sigma = \sigma_1 - j\sigma_2$, into equations 2.15 and 2.17, resulting in

$$Z_s = \sqrt{\frac{j\omega\mu}{(\sigma_1 - j\sigma_2)}} \tag{2.18a}$$

$$\gamma = \sqrt{j\omega\mu(\sigma_1 - j\sigma_2)} \tag{2.18b}$$

where the conduction current, $\sigma \gg \omega\epsilon$

2.2.3 Nonlinear Response

Nonlinear properties of superconductors represent an important limitation of the performance and application of superconducting devices at microwave frequencies. Based on the phenomenological theory, the nonlinear surface impedance, $Z_s(H_{RF})$ is dependent on the RF magnetic field, H_{RF}, or alternative the current J_{RF}, of the material. This is known as the power dependence because it is observable, in a superconductor, as a response to a change in power. The surface impedance in equation can be rewritten as

$$Z_s(H_{rf}) = R_S + jX_s \tag{2.19}$$

where the dependence of H_{RF} is introduced to the surface resistance, R_S, and reactance, X_S. AN expression for R_s and X_s can be derived from the two-fluid models as

$$R_s = \frac{\mu_0^2 \omega^2 \lambda^3 \sigma}{2} \tag{2.20a}$$

$$X_s = \omega \mu_0 \lambda \tag{2.20b}$$

where λ and μ_0 are a function of the RF magnetic field, H_{RF}.

Chapter 3

Resonator Fabrication and Experimental Methods

3.1 Birdcage Resonator Fabrication

The substrate on which the birdcage is fabricated is a double-side polished, 430 micron thick, 2 inch C-cut sapphire wafer. The wafers are sourced from CrysTec Inc. C-cut wafers are chosen in order to reduce the lattice mismatch of the deposited Niobium, which can have detrimental effects on the superconducting properties of the grown films [20]. The wafers, according to the CrysTec datasheet, have a dielectric constant of 11.25. The high dielectric constant makes sapphire a good candidate as a low loss substrate. Table 3.1 outlines the properties and their corresponding values of the wafer.

Property Name	Value
Dielectric Constant	11.25
Dielectric Strength	4.8 $\times 10^4$ kV/m
Loss Tangent	$< 10^{-4}$
Resistivity	10^{14} (25 C)
Thermal Expansion	5.3 $\times 10^{-6}$ K^{-1} (25 C)

Table 3.1: *The properties, and associated values, of the CrysTec sapphire wafer used for fabrication.*

The deposition of niobium onto sapphire is an established procedure in our lab. A series of resonators, which form the cells of the birdcage, are fabricated on the top-side of the wafers. The films are deposited using the Omicron ultra-high vacuum (UHV) sputtering chamber, show in figure 3.1. The wafer is patterned and diced in the Quantum Nano-Fabrication Laboratory (QNF) at the University of Waterloo.

Prior to the niobium film deposition, each wafer underwent a combination of solvent and

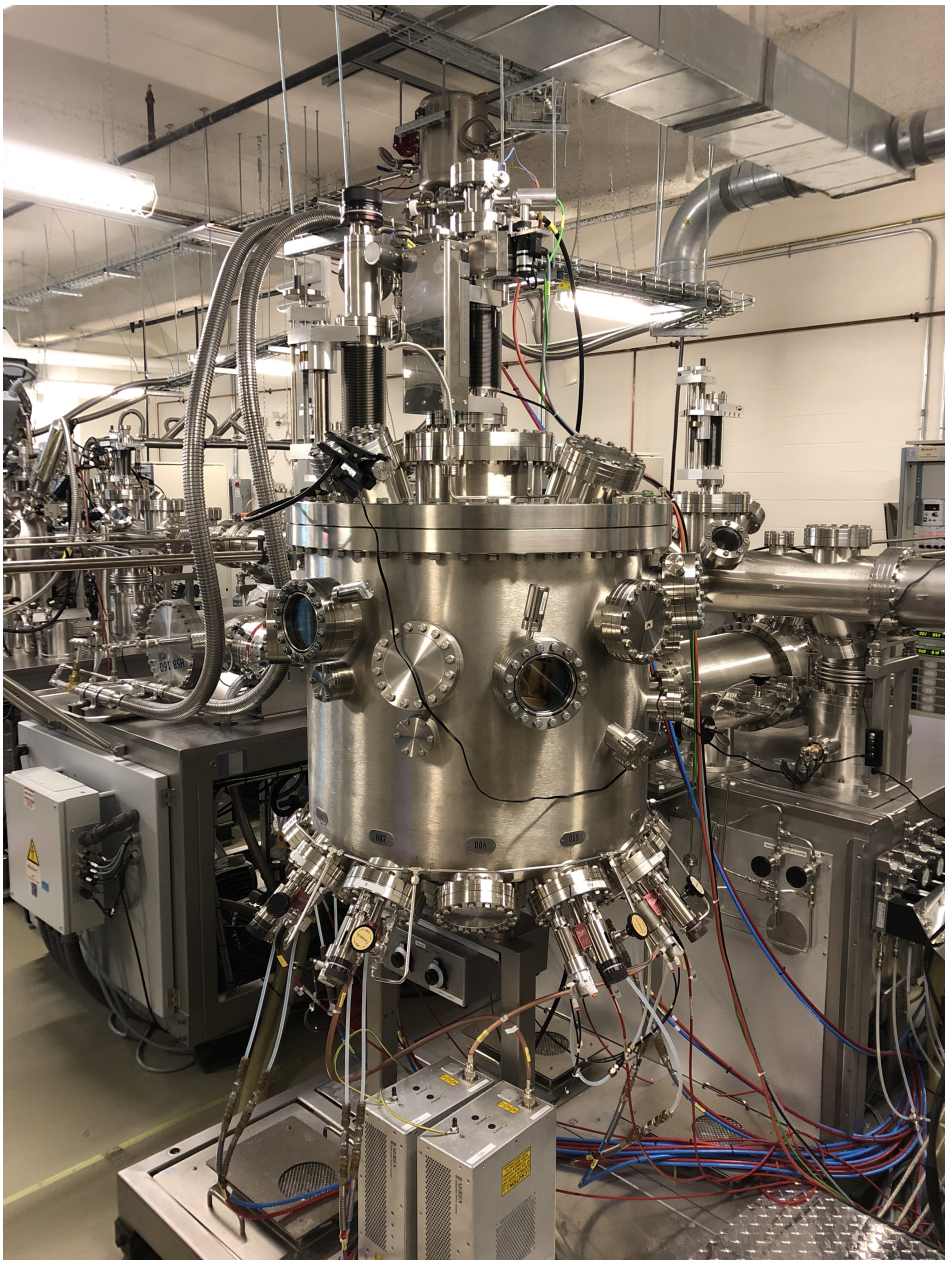

Figure 3.1: *Omicron UHV sputtering system used to deposit Niobium films onto the sapphire wafers.*

acid cleaning. This removes organic and water-soluble materials from the surface of the wafer in order to enhance the adhesion of the deposited film. The cleaning procedure is as follows:

1. Ultrasonication for 15 minutes in 250mL beaker of Acetone
2. Ultrasonication for 15 minutes in 250mL beaker of Isopropanol (IPA)
3. Repeat steps 1 and 2

4. Soaked in 500mL beaker of Piranha solution for 10 minutes
5. Rinse with DI water in empty 500mL beaker
6. Dry with N_2 gas, held with tweazers in empty beaker

The omicron cluster tool is a multi-stage system, where the sapphire wafer can be transferred between different sputtering and characterization chambers without breaking vacuum. The pressure inside the omicron system reaches 3×10^{-10} mBar, and the wafer is moved using a rail line that spans the length of the system. Magnetic arms are used to transfer the wafer into the corresponding sputtering chambers and loaded onto the wafer mount. After cleaning, the wafer is transported in a vacuum sealed bag to the load-lock of the system. The wafer is then heated for approximately 2 hours at $150 - 200$°C to desorb water from the surface and holder assembly before being moved to the metal oxide chamber. Once there, the wafer is annealed four times using the resistive heating and quenching procedure as follows:

1. Heated at 600°C for 30 minutes
2. Annealing at 1000°C for 3 minutes
3. Allow chamber to cool down back to 600°C and pressure to recover to 10^{-9}mBar
4. Repeat steps 1-3, four times

The deposition took place within the superconducting sputter chamber, where a base pressure below 10^{-10} mBar is maintained. This module is occupied with DC power supplies to deposit high purity Niobium. A quartz micro balance is used to verify the deposition rate prior to the deposition. After the clean sapphire wafer is been transferred to the this chamber, the temperature of its surface is set to 770°C and the sample is rotated at a rate of 15 rpm. After the temperature reaches the set-point, an Argon gas flow of 30 sccm is introduced, and the DC power supply is set to 200 watt. The system is left to stabilize for 30 min in order to get remove any oxide build on the Nb target. The deposition is then monitored with the quartz micro balance, which was at a rate of 17 nm/min, and ran for a total of 10 minutes. The wafer is then allowed to cool, and the total thickness of the grown film is approximately 100 nm.

3.1.1 Photolithography

After the niobium film is deposited, the wafer is transferred back to the QNF for patterning. To fabricated the resonators, the sample is put through a multi-step process of optical lithography and dry etching, shown in figure 3.2.

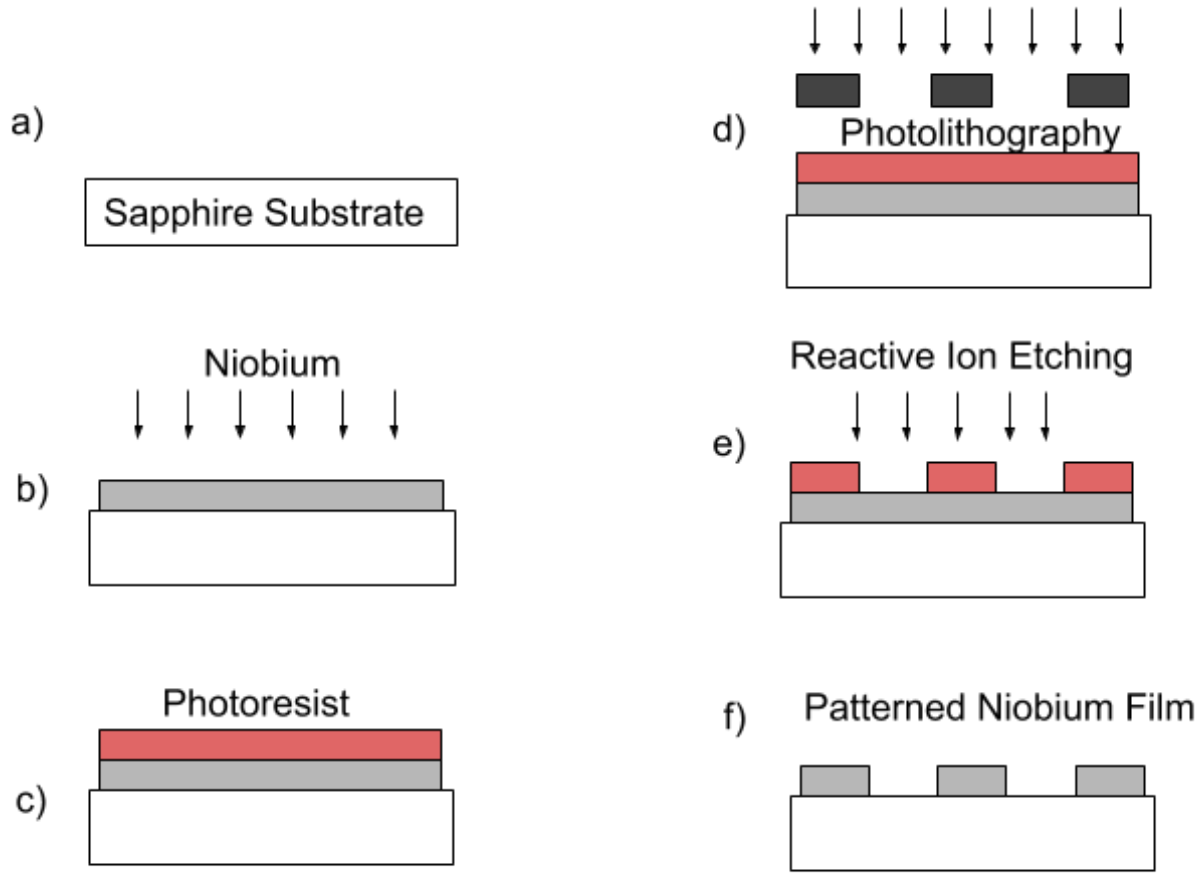

Figure 3.2: *Outline of the process used to fabricated the birdcage resonator a) a blank, 2 inch, 430 microns thick sapphire wafer is cleaned and placed within the sputtering chamber of the omicron UHV system, b) 100 nm of Niobium is deposited on the top surface of the sapphire wafer, c) the wafer is transported to the QNF where a 500 nm thick layer of photoresist is spin coated onto the wafer, d) exposed for 2.7 seconds at a lamp power of 380-420W to imprint the resonator design, e) dry-etch RIE to remove undeveloped resist areas, to reveal f) the final resonator pattern.*

The design of the resonator is illustrated in figure 3.3. The photolithographic mask used to fabricate the resonators is designed with AutoCad, and machined at Toppan Photomasks Inc. There are two sizes of the resonator design that make up the birdcage. The leg element is represented by the elongated conductor that extends parallel to the length of the resonator. The ring element is represented by two conductor strips along the width of the resonator, perpendicular to the leg. The width and length of the first resonator design is 10mm and 27mm, respectively. The length of the second resonator matches the first, however, the width is large at 10.86mm. The purpose of this variation for ease of assembly and so the smaller resonator can fit inside and secured to the larger resonator while construction the 3D resonator. The leg elements measure 23.7mm long and 0.15mm wide, the rings

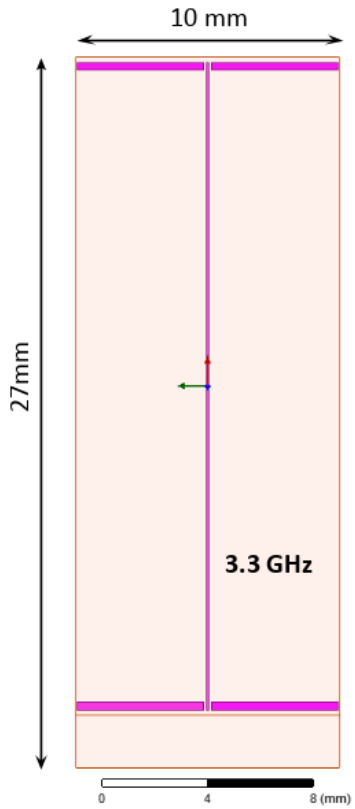

Figure 3.3: *The resonator design fabricated on a 430 micron thick sapphire wafer measuring 27mm in length, and 10mm in width. This design is one of two which makeup the birdcage resonator. The second design has a larger width at 10.86mm, illustrated below in figure 3.3. The smaller resonator is intended to fit in between the edge of the wafer and the beginning of the niobium conductor.*

are 4.85mm long and 0.3mm wide, in both designs. The gap between the legs and the rings are 100nm.

Before coating with photoresist, the wafer is dehydrated on a hot plate at 90°C and allowed to cool for 1 minute. A positive ultraviolet (UV) photoresist, Shipley 1805, is spun onto the wafer at 4000 rpm, for 90 seconds, for a thickness of 500 nm. The resist is then soft baked on the hot plate at 90°C for 1 minute. Once it has cooled, the sample is transferred to the Karl Suss MA6 Photolithographic system and put into soft contact mode. The mask is aligned to the wafer and the wafer is exposed for 2.7 sec at a UV lamp power of 380-420W to pattern the resist.

Next, the resist is developed and etched. The wafer is placed inside a 250mL beaker of MF319 developer, and gently agitated for 40 seconds. The wafer is rinsed with DI water for 1 minute and blown dry with nitrogen gas. The sample is then etched using the Oxford PlasmaLab System 100ICP380 for reactive ion etching (RIE). The action of RIE is to remove any undeveloped resist and reveal the full features of the resonator. The recipe used is a dry etch of niobium with Argon and SF6, where the etch rate is 0.75 nm/s, for a total

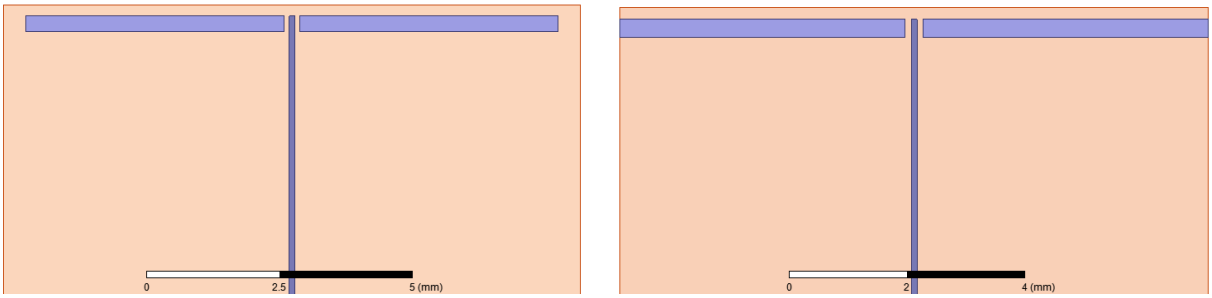

(a) **(b)**

Figure 3.4: *An enhanced view of the two resonators. Resonator a) has a width 10.86 mm and b) 10 mm. The wider of the two resonators, (a), has a 430 micron gap at the edge of the wafer in order for resonator (b) to make a seamless connection. The gap between the ring conductors and the center conductor, in both designs, is 100 nm.*

of 4 minutes. If any excess resist remains, the resonators are stored overnight in a beaker of acetone, which helps to breakdown the resist. On the following day, the resonators are ultrasonicated in acetone and IPA for 10 minutes. The agitation removes any excess resist still on the wafer. The sample is blown dry with nitrogen and stored in a vacuum bag.

3.1.2 Dicing

After the sample has been fully developed, and any excess resist has been removed, the wafer is then diced into the resonator which make up the birdcage. The wafer is first coated with photoresist to protect it from any broken particles during dicing. The wafer is dehydrated on a hotplate, set to 90°C, for 1 minute and allowed to cool for an additional minute. The wafer is then coated with 1100 nm of Shipley 1811 photoresist and soft baked for 1 minute at 90°C. The wafer is then transferred to the packaging lab of the QNF, and mounted into the DISCO DAD3240 automatic dicing saw. In order to dice the wafer, a total of 3 passes must be made with the VT07 blade, from disco, due to the thickness of sapphire wafer. The blade uses a vitrified bond that allows for high precision dicing of sapphire. The diced resonators are then transferred into a clean container where the resist is removed by a rinse with acetone and IPA. The resonators are again stored in a vacuum bag.

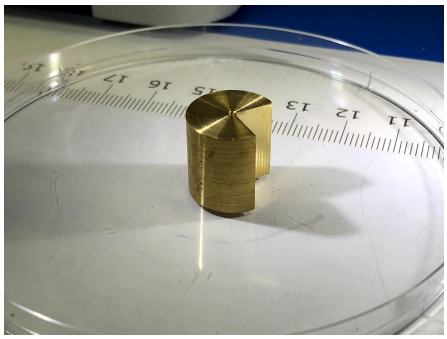

Figure 3.5: *The two accessory components used in the assembly of the birdcage resonator. a) NOA81 is a single component, polymer-based, liquid adhesive used to secure the individual resonators together. b) the 90 brass wedge used to align the resonators together.*

3.1.3 Resonator Assembly

After the wafer has been diced, the individual resonators are assembled into the birdcage device. Two accessory components are used in the assembly: Norland Optical Adhesive 81 (NOA81), shown in figure 3.5, and a brass 90 degree wedge, shown in figure 3.5. NOA81 is a single component, polymer-based, liquid adhesive that when exposed to ultraviolet (UV) light, cures into a hard polymer. The brass wedge is used, under a microscope, to align the rings of the resonators, and in combination with a dab of the adhesive, to assemble the birdcage structure.

3.2 Experimental Setup

3.2.1 Vector Network Analyzer

A N5230A PNA-L Network Analyzer is used to perform the measurements reported in this thesis. The resonator is excited using a two-port measurement scheme and characterized by transmission measurements. Electrical coupling is accomplished using two feed-lines loops positioned opposite each other and aligned to the center of the leg of the birdcage, as shown in figure 3.6. The loops are made from the inner conductor of RG-405 flexible semi-rigid coaxial cable. The inner conductor is made from copper clad steel, spaced with PTFE dielectric, and has an impedance of 50 Ohms. The maximum frequency of the cable is 40 GHz.

Two, six-foot, coaxial cables are used to connect the VNA to the birdcage. The cables are

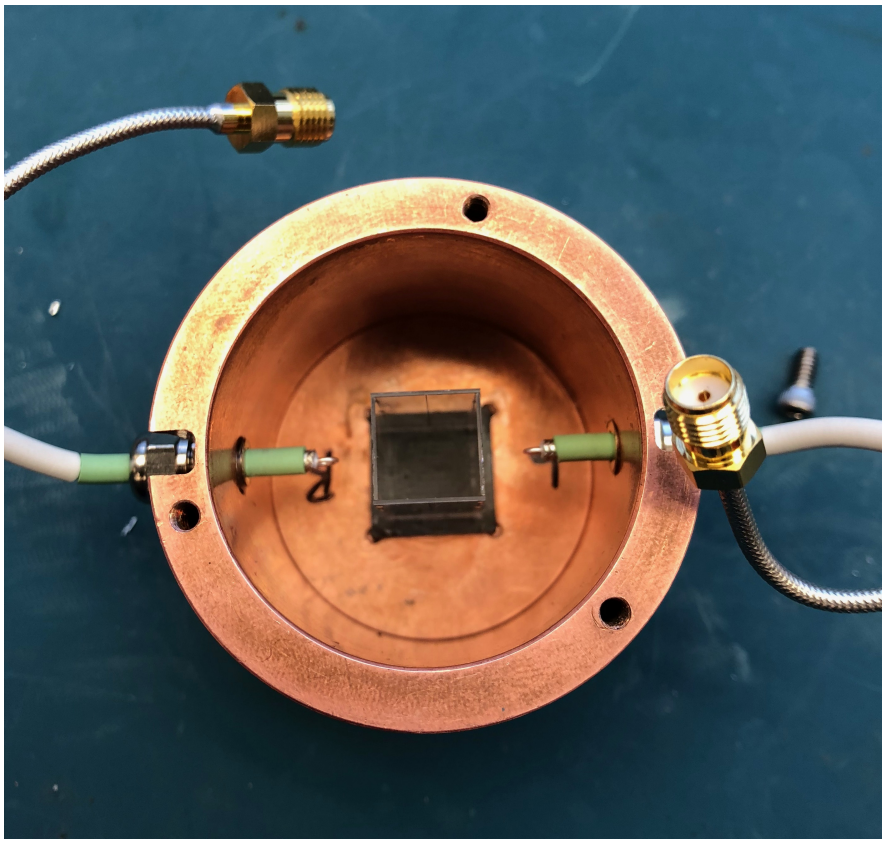

Figure 3.6: *A top down view of the empty birdcage resonator placed within a custom copper packaging. The resonator measures 27 mm in height, 10.86mm in width, and 10mm in length. The resonator package is 40mm in diameter and 40mm in height. The two feed-line loops, positioned on opposite sides and separated by a 5mm gap to the face of the resonator, are used to couple into the resonator. The loops are made from the inner conductor of the feed-line loops, soldered to its outer shield. The diameter of the loops are 0.36mm and the length is 20mm. The feed-lines are made from RG-405 semi-rigid coaxial cable purchased from Pasternack.*

first attached to the VNA and then connected to the top of the low temperature probe, which is connected to the birdcage. The entire setup is illustrated in figure 3.10. The length of the cables is calibrated to the VNA, using a microwave calibration set. A full two-port calibration is done to well defined standards using the short-open-load-thru (SQLT) calibration algorithm. The short termination is defined by a frequency-dependent inductance, and the open is defined by a frequency-dependent capacitance. A fixed 50 ohm load is used to load match the cables, and the through is used for calibrating the transmission. This procedure eliminates sources of noise, and error, that may arise due to the signal transmitted along the length of the cables. The calibration is done at room temperature.

3.2.2 Resonator Package

A copper package is designed to act as both a shield, protecting the birdcage from external sources of noise, and to house the birdcage when submerged in the liquid helium dewar. The package is machined from oxygen-free high thermal conductivity (OFHC) copper. It is constructed from three separate pieces: a top plate, a bottom plate, and a body, shown in figure 3.7. The top and bottom plates measure 50 millimeters in diameter, and are machine with a lip to secure the plates to the body. The bottom plate is machine with an additional 11 by 11 millimeter in crevice, in order to fix the resonator to the bottom. The body of the package measures 40 mm in height and a diameter of 40 mm. Both the top and bottom lip are used to fix the plates and enclosing the birdcage. The size of the package is such that its resonance frequency are beyond that of the birdcage and will not interfere with the measurements.

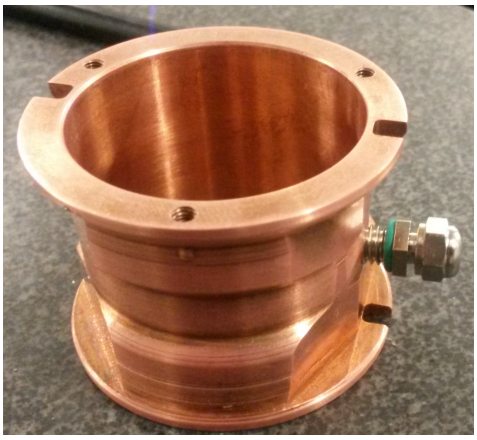

(a)

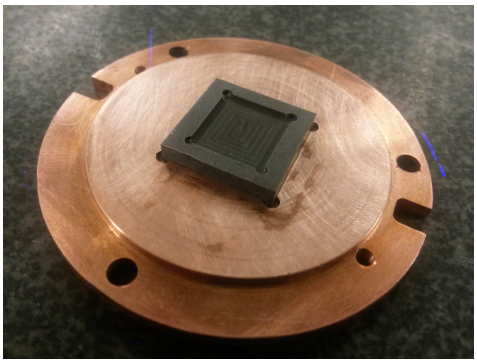

(b)

Figure 3.7: *The copper package designed to house the birdcage resonator in the liquid helium dewar. The body of the package, (a) measures 40 mm in height, with an inner diameter of 39mm and outer diameter of 40mm. The wall thickness, as measured at the center of the package, is 1mm. The plate, shown in (b), is 42mm in diameter, including the lip to connect to the body of the package. The inner platform is 39mm in diameter and 2mm in height.*

The birdcage is not directly glued to the bottom plate of the package. A Roger laminate, a ceramic filled PTFE composite material designed for high frequency applications and designed not to interact with the resonator, is machine with a crevice to secure the birdcage as shown in figure 3.7. The crevice measures 11 by 11mm and 1mm deep, slightly larger than the birdcage. The birdcage is fixed to the laminate with Loctite 409, an industrial adhesive.

Two additional holes are drilled into the side of the package to insert the feed-line. Brass cord grips, with an outer diameter of 6mm, are placed within these holes to fix the feed-lines in place. The cord grips are nickel plated for corrosion resistances. They use a rub-

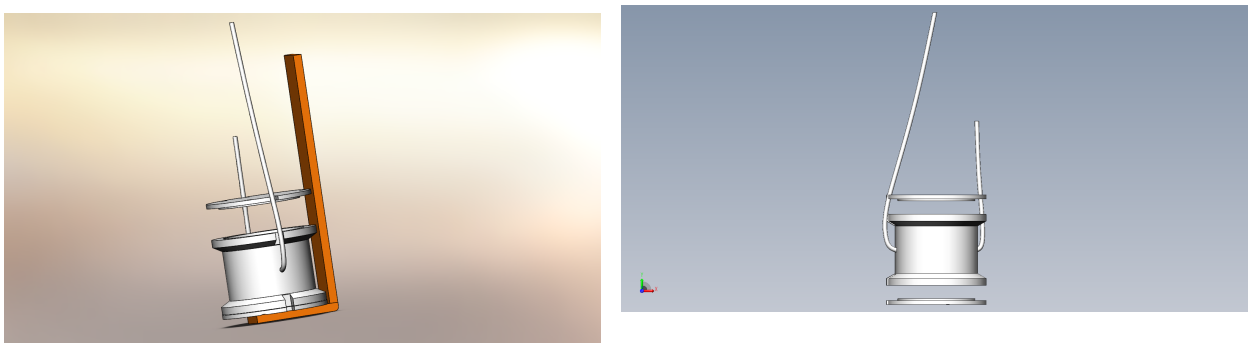

Figure 3.8: *The full CAD model of the birdcage package, along with coaxial feed-line cables, attached to an L-bracket. The L-bracket is used to secure the package to the low temperature probe. The bracket measures 15cm in height, with a thickness of 2mm, and a length of 45mm. The coaxial feed-lines are 20 mm in length, and extend from the body of the package to the coaxial connectors of the probe.*

ber bushing and 3.175 mm O-ring, on the inside of the cord grip, are used to create a tight seal around the feed-lines. The distance between it and the legs of the birdcage can be manipulated by tightening and loosening the grips. The cord grips and the complete package design and feed-lines are shown in figure 3.8

3.2.3 Low Temperature Probe

The low temperature probe, shown in figure 3.9, is constructed from a 6 foot long stainless steel rod. The probe acts to support the copper package when submerged in liquid helium. At the base of the probe is a 15 cm copper sheet used to mount the L-bracket, which the copper package is attached. There are a total of two feedthroughs at the top of the probe which are used to connect the VNA to the feed-lines.

Figure 3.9: *Low temperature probe*

3.2.4 Liquid Helium Dewar

Experiments are performed with a liquid helium (LHe) dewar from Precision Cryogenic. The dewar may contain up to 100 litres of LHe. While submerged in LHe, the temperature for experiments is maintained at 4.2 Kelvin. The dewar has a 3 inch, inner diameter, opening at the top which is used to lower the probe to its base.

3.3 Experimental Procedure

The typical experimental procedure begins by bringing the resonator into a superconducting state. The resonator is submerged into liquid helium, using the low temperature probe, where it reaches a temperature of approximately 4 Kelvin. The coupling, and subsequent excitation, by feed-line loop is used to operate the resonator. Transmission measurements, S_{21}, are then used to characterize the quality factor of the resonator.

Three different experimental configurations are used to characterize the birdcage resonator. Initially, the separation between the feed-line loops and the resonator legs is adjusted to measure the maximum quality factor of the empty birdcage. The power and magnetic field dependence are also measured. The birdcage is then perturbed using an aluminum ball bearing and aluminum sheet to investigate the magnetic field produced by the birdcage. The experimental results are presented in the following section.

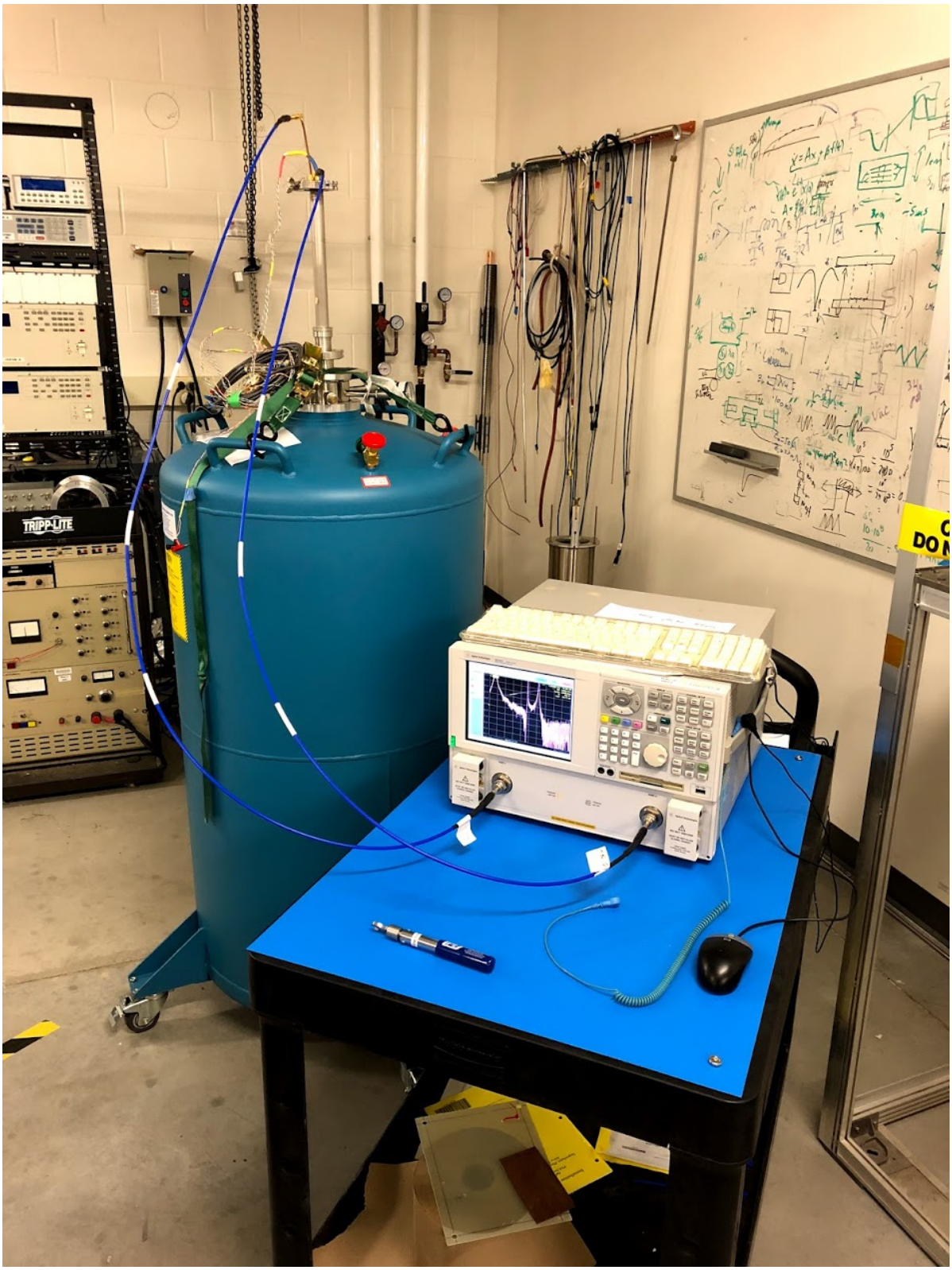

Figure 3.10: *The complete experimental setup used to characterize the Birdcage resonator. The two-port VNA is connected to the birdcage resonator via coaxial cables attached to the low temperature probe at the top of the Helium Dewar.*

Chapter 4

Experiments and Results

4.1 Circuit Analysis of Birdcage Resonator

4.1.1 Lumped Element Eigenanalysis

The birdcage resonator can be modeled as a linear network of identical cells. Each cell is composed of two leg and ring elements. Each cells is effectively a resonator. The network is a periodic arrangement of these cells, which may be modeled as a series of inductive and capacitive elements, and the mutual inductance between the elements is ignored. We evaluate the network using mesh analysis to derive a set of linear equations describing the modes of operation of the resonator [6, 21, 17].

The ladder network representing the band-pass resonator, with N-legs, is shown in figure 4.1. The analysis is done by applying Kirchhoff's voltage law to each of the N total cells

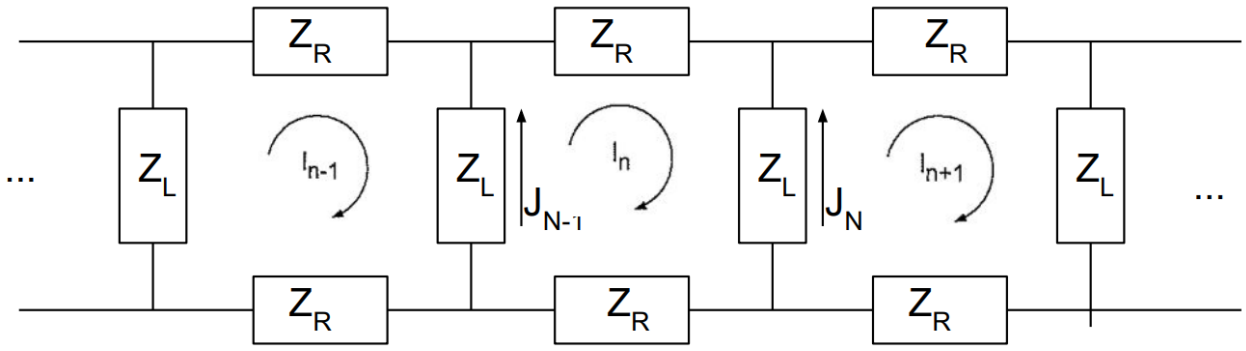

Figure 4.1: *The ladder network representing the birdcage resonator. Each cell is composed of two leg elements Z_L, and two ring elements Z_R. The network is symmetric [6].*

and is solved as a generalized eigenvalue problem. The impedance of the leg and rings are labeled as Z_L and Z_R respectively,

$$Z_L = j\omega L_L + \frac{1}{j\omega C_L} \tag{4.1a}$$

$$Z_R = j\omega L_R + \frac{1}{j\omega C_R} \tag{4.1b}$$

where L_L and C_L are the inductance and capacitance of the legs, L_R and C_R are the inductance and capacitance of the end-rings. The voltage of the n^{th} mesh is written as

$$Z_L(I_{n+1} + I_{n-1}) - 2I_n(Z_R + Z_L) = 0 \tag{4.2}$$

where n is the current mesh, between 0 and N-1, and I_n is the current of the n^{th} mesh. Expanding to the entire network, equation 4.2 can be written in matrix form as

$$\begin{bmatrix} 2(Z_L+Z_R) & Z_L & 0 & \dots & Z_L \\ Z_L & 2(Z_L+Z_R) & Z_L & \dots & 0 \\ \vdots & \dots & \ddots & & \vdots \\ Z_L & \dots & \dots & & 2(Z_L+Z_R) \end{bmatrix} \begin{bmatrix} I \\ \vdots \\ I_N \end{bmatrix} = 0 \tag{4.3}$$

The mesh and leg currents are related by $J_n = I_n + 1 - I_n$, where J_n is the current in the leg of the n^{th} mesh. The periodicity of the network means $I_n = I_{N-n}$, and the matrix is circulant [6, 17]. Taking the determinant of 4.3 a solution to the matrix can found analytically, where the eigenvalues are the resonant frequencies and eigenvectors are the mesh currents of the network.

The j^{th} eigenvector and eigenvalue are found analytically to be

$$v_j = [exp(\frac{j2\pi}{N})^0 exp(\frac{j2\pi}{N})^1 \dots exp(\frac{j2\pi}{N})^{N-1}] \tag{4.4a}$$

$$\lambda_j = -2(Z_R + Z_L) + Z_L(exp(\frac{j2\pi}{N}) + Z_L exp(\frac{j2\pi(N-1)}{N}) \tag{4.4b}$$

The j^{th} resonant frequency are found by setting $\lambda_j = 0$

$$\omega_j = \sqrt{\frac{C_R^{-1} + C_L^{-1}[1 - cos(\frac{2j\pi}{N})}{L_R + L_L[1 - cos(\frac{2j\pi}{N})}} \tag{4.5}$$

corresponding to the current distribution in the leg elements. The eigenvectors are found to be

$$W_j = 2isin(\frac{j\pi}{N})exp(\frac{j\pi i}{N})v_j \tag{4.6}$$

for $j = 0, 1, \ldots, N-1$.

4.1.1.1 Perturbation

While the analytical description provides a tool for predicting the resonant frequencies the solution is limited to the assumption of perfect assembly of the birdcage. Perfect assembly is defined here as the precise alignment of each resonator face in the construction. As each face is glued by hand, misalignment of the end-rings between each face is possible leading to a gap in between adjacent resonator faces, and with it capacitance values which vary from the desired value. Therefore, the eigenanalysis is repeated with the addition of a perturbation parameter, introduced into the ring capacitance. The perturbation removes the circulant property of the matrix, and a solution is found numerically [17]. The ring impedance of a misaligned face can be written as

$$Z_\delta = j\omega L + \frac{1}{(j\omega C)(1-\delta)} \tag{4.7}$$

where δ is the perturbation parameter, $0 \leq \delta < 1$. In the case of the fabricated four-leg birdcage resonator, the matrix can be rewritten as

$$\begin{bmatrix} 2Z_L + Z_R + Z_\delta & Z_L & 0 & Z_L \\ Z_L & 2(Z_L + Z_R) & Z_L & 0 \\ 0 & Z_L & 2(Z_L + Z_R) & Z_L \\ Z_L & 0 & Z_L & 2(Z_L + Z_R) \end{bmatrix} \tag{4.8}$$

and is solved numerically using mathematica. The change in the resonant frequency of the transverse mode, with respect to δ, is shown in figure 4.2. Introducing a perturbation has the effect of increasing the resonance frequency of the transverse mode. The gap may increase the capacitance of the ring, and therefore the resonant frequencies of the transverse mode.

This analysis may be further expanded by replacing the ring impedance in any mesh with the perturbation impedance in equation 4.7.

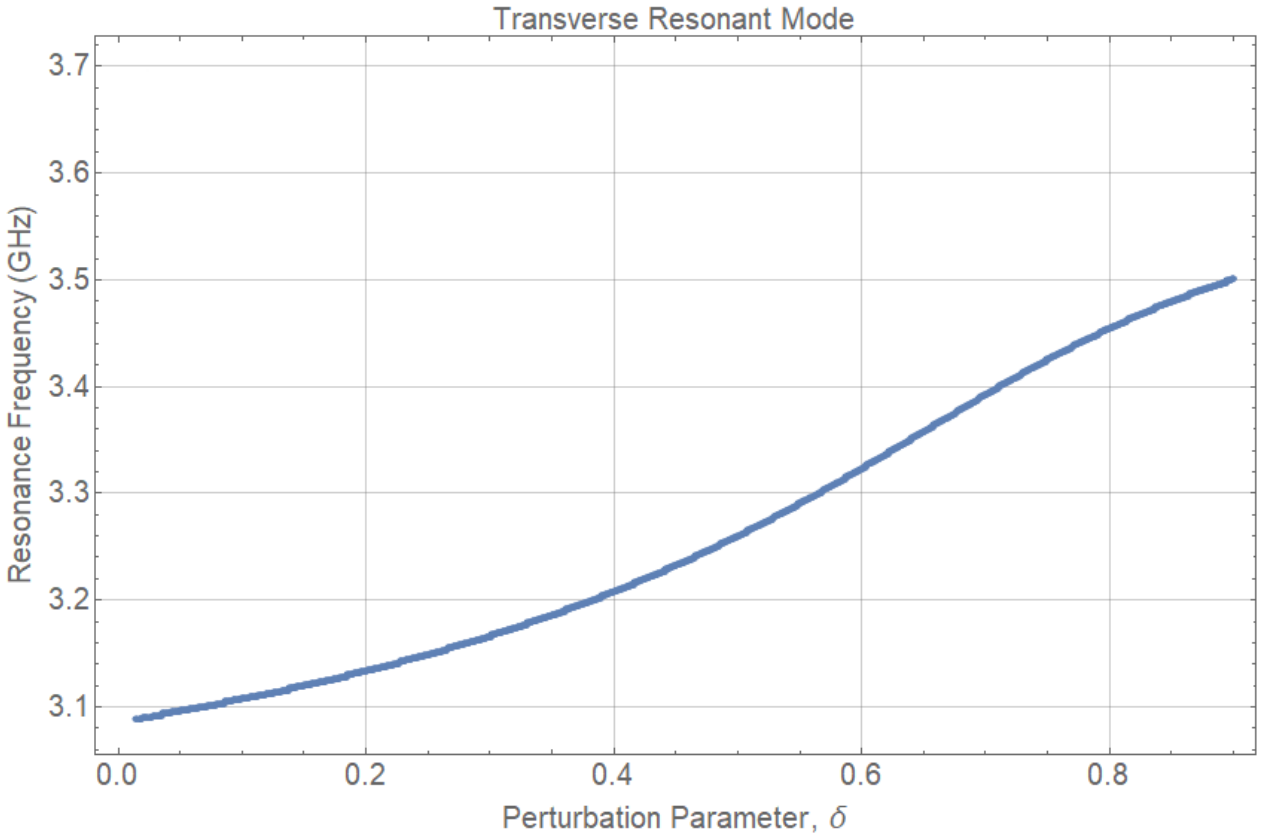

Figure 4.2: *Perturbation of the resonant frequency of the transverse mode. The perturbation parameter δ is varied from 0 to 1.*

4.2 Experimental Results

4.2.1 Empty Birdcage Resonator

In this experiment, the empty birdcage, shown in figure 4.3, is characterized. The separation between the feed-line loops and the resonator legs, as it relates to the quality factor, is measured. These values are used to find the optimal gap at which the loops are fixed for the rest of the experiments. The power and magnetic field dependence of the birdcage are also measured.

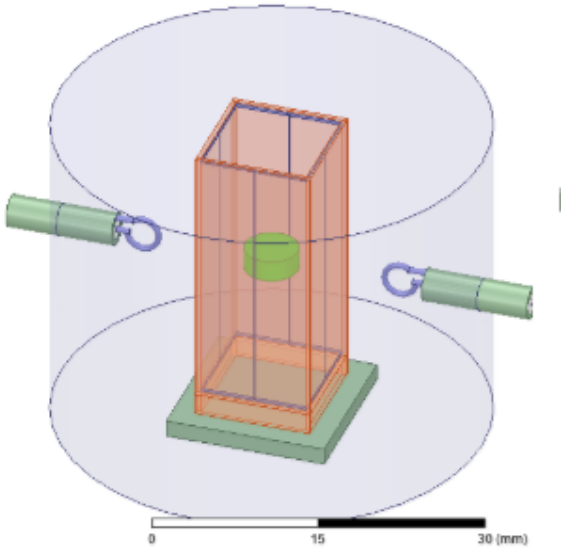

Figure 4.3: *A side view of the empty birdcage resonator, secured within the copper package, as modeled in HFSS. The birdcage is fixed to the rogers laminate at the base of the package and centered inside the package. The gap between the feed-line loops and resonator legs is initially fixed at 4mm. The cord grips, not shown here, can be adjusted to increase or decrease the gap.*

4.2.1.1 Simulated Field Distribution

The distribution of the magnetic field, created in the empty birdcage resonator, is simulated using Ansys HFSS and shown in figure 4.4. The quality factor is $Q = 5768$, and the resonant frequency $f_0 = 3.02$ GHz. The arrows indicate the magnitude and direction of the

field within the resonator. The two-port excitation of the resonator creates a linearly polarized magnetic field in the direction perpendicular to the feed-line loops.

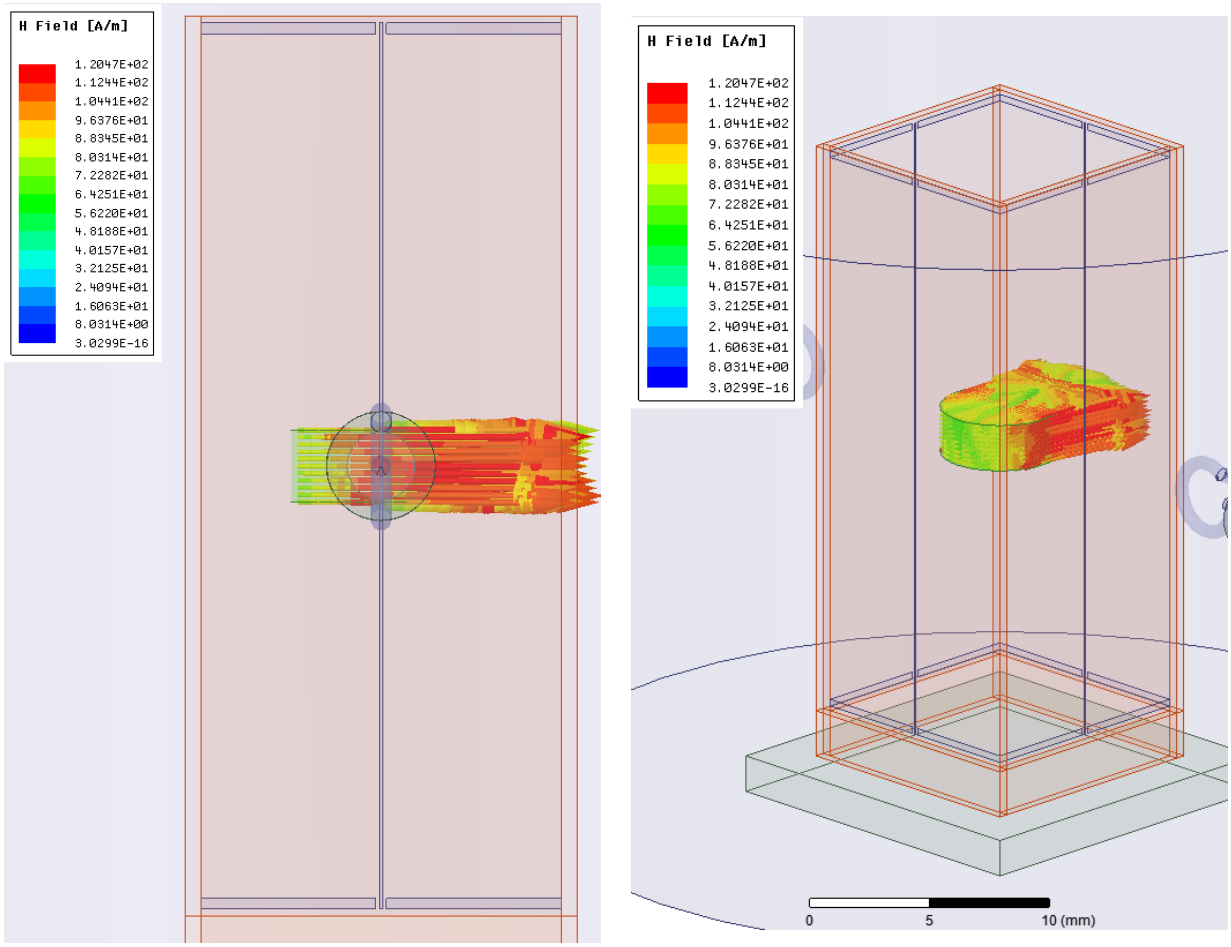

(a) **(b)**

Figure 4.4: *The magnetic field distribution within the empty resonator, as simulated in HFSS. The resonator generates a magnetic field in the direction perpendicular to the feed-line loops. The sample, in the center, is simulated as lossless. The input power is* P_{in} *= 1 W, and* s_{21max} *= -0.94dB. The Q of the simulated resonator is 5768 and* f_0 *= 3.019425*

4.2.1.2 Quality Factor

The quality factor, Q, of the empty resonator is measured with respect to the separation between the feed-line loops and its legs. Initially, they are brought close to one another, approximately 4mm apart, where the resonator is strongly coupled to the feed-lines and the Q measured is 3450. The separation is then increased to a maximum separation of 7mm, whereby coupling is reduced and the Q measured is 4150. The magnitude of S_{21},

measured quality factor, resonance frequency, and loss for various separations are shown in figure 4.5 and table 4.1, respectively.

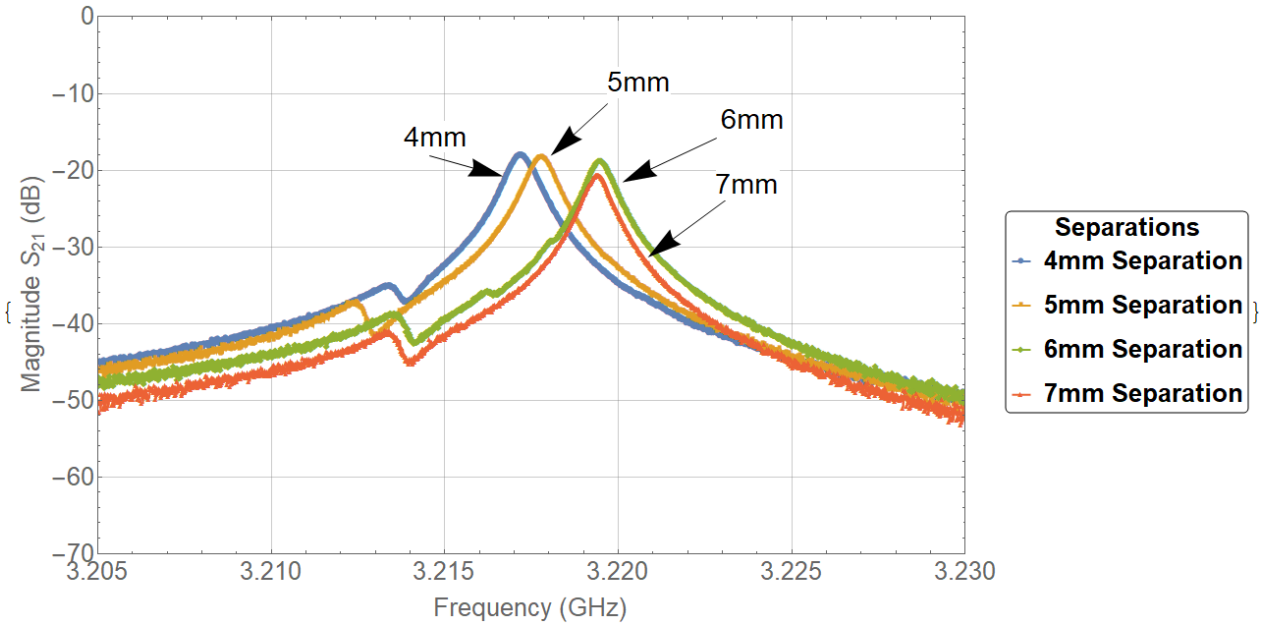

Figure 4.5: *The transmission, S_{21}, measurement of the transverse mode of the empty birdcage resonator. The separation distance is measured from the outside face of the resonator to the feed-line loop. The separation is varied, beginning at 4mm, up to a maximum of 7mm. The quality factor of the resonator is measured using the 3dB method. Higher separation distances is observed to increase the measured Q.*

From the transmission measurements, we observe a modest increase in Q from 3450 to 4150. An increase in the separation causes the external quality factor, Q_e, to increase. Based on the relationship between the total and coupling quality factors, the measured Q becomes higher by reduced coupling to the resonator. This gives a closer measurement to the internal quality factor, Q_i. In comparison to the simulated Q of 5768, our experimental results show that there is room for improvement. The radius of the copper package can be increased, and the feed-line loop pulled further back, to increase the measured Q. In addition, coupling between the feed-lines is observed, between 3.210 and 3.215 GHz, at the tail of the resonance peak.

Separation (mm)	Q	f_0 (GHz)	Loss (dB)
4	3450	3.2172	-18.0871
5	3700	3.21782	-18.3857
6	4000	3.21948	-18.7993
7	4150	3.21944	-20.6542

Table 4.1: *Measured value of Q, resonant frequency f_0, and microwave loss at variable separation of the feed-line loops to the resonator.*

4.2.1.3 Power Dependence

We examine the power dependence of the resonant frequency, and quality factor by varying the input microwave power from -30dB to -10dB. At higher microwave power, however, the resonance curve can no longer be approximated as Lorenztian and the measurement of Q may not be accurate. The transmission measurement, and measured value of Q, are shown in figure 4.6 and table 4.2.

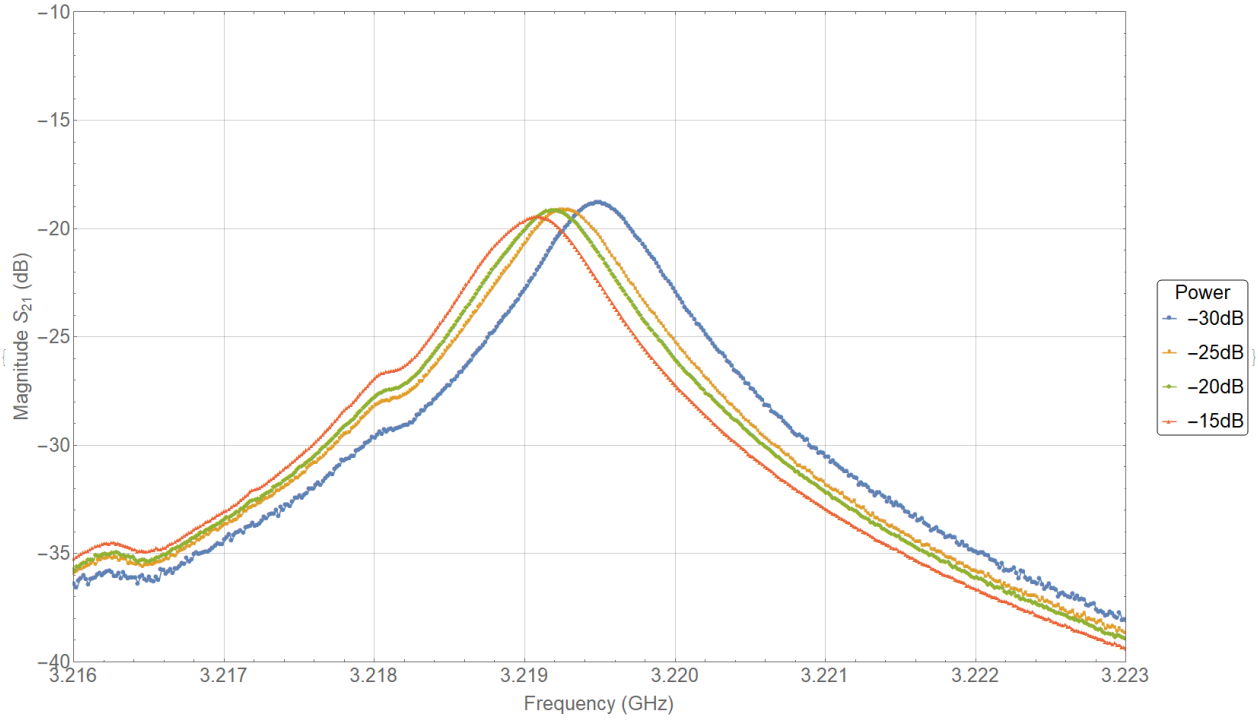

Figure 4.6: *Transmission measurement of the transverse mode taken at difference input microwave powers, from -30dB to -10dB. The power dependent measurement is used to observe the non-linearity of the resonator. At powers greater than -10dB, the shape of the resonant curve is no longer Lorenztian.*

Beginning with increased microwave power, from -30 to -15dB, both the resonance curve broadens and the frequency shift to lower values. The shift in resonant frequency is a result of increased kinetic inductance of the resonator and accompanied by a change in quality factor of the resonator. The relative change in frequency is defined as $\Delta f_0/f_0 = [f_0(P_{min}) - f_0(P)]/f_0(P_{min})$, and the change in Q as $\Delta Q = Q(P) - Q(P_{min})$. The dependence of Q and $\Delta f_0/f_0$ on the input microwave power P_{in} is show in figure 4.7. A relative shift of 0.000425 between -30 dB and -10dB with a decrease in Q from 3987.67 to 2821.95, is observed. A coupling between the feed-lines is still observable at the tail of the resonance peak, at all power levels. An additional peak, closer the resonance peak, is also observed, and the result of which maybe from material imperfections or film degradation of the resonator.

P_{in} (dB)	Q	f_0 (GHz)	Loss (dB)
-30	3987.67	3.21948	-18.7993
-25	3816.41	3.21926	-19.1517
-20	3815.34	3.21919	-19.1573
-15	3621.41	3.21908	-19.4627
-10	2821.95	3.21879	-21.7944

Table 4.2: *Measured values of Q, resonant frequency f_0, and loss at varied input microwave power P_{in}.*

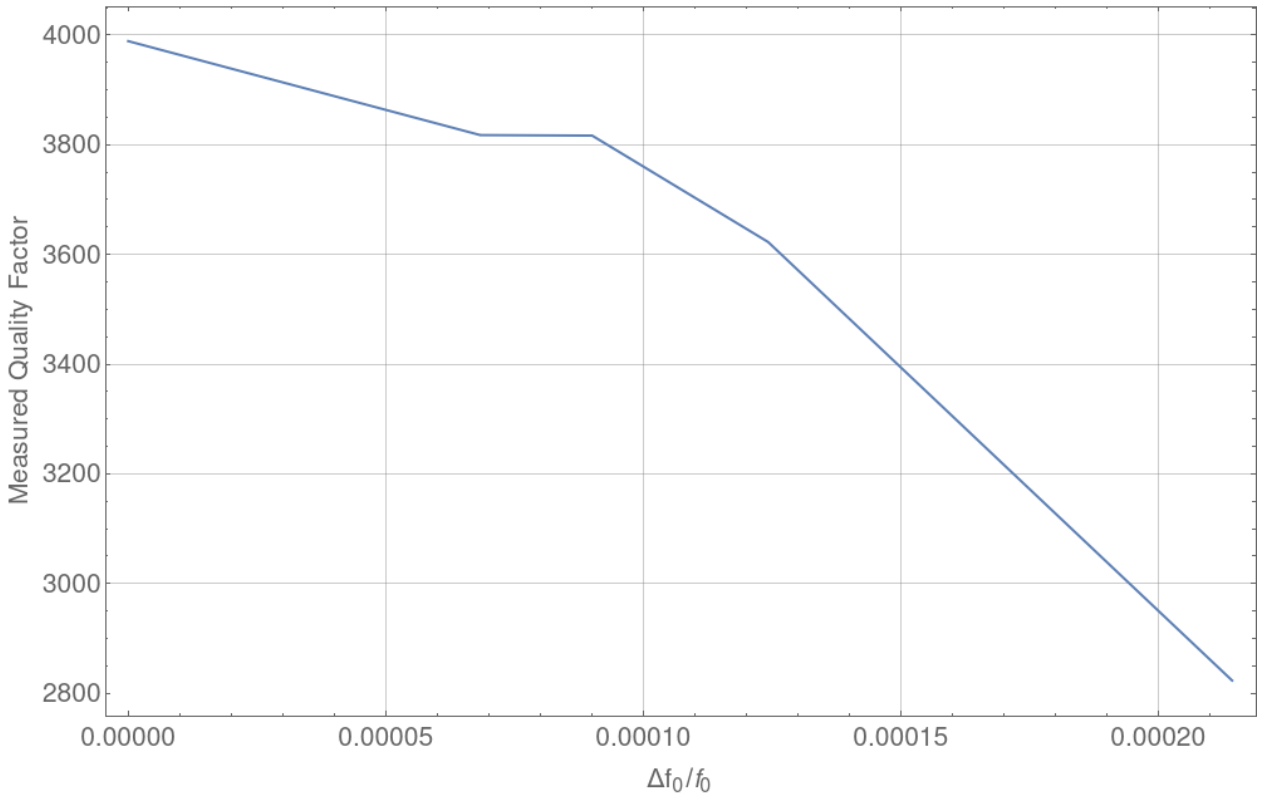

Figure 4.7: *Plot of Q vs $\frac{\Delta f_0}{f_0}$ of the empty birdcage resonator. The results show the decrease in quality factor with an increase in relative shift of the frequency at higher microwave power.*

4.2.1.4 Magnetic Field Dependence

The magnetic field dependence of the quality factor is examined here. The resonator is placed within a low temperature dewar, from Cryomagnetic Inc., where an external field is applied parallel to the resonator's z-axis. We note here, however, that the orientation of the resonator to the field is not perfect, and a misalignment may exist. The field strength is then increased from 0 to 0.9 Tesla. The feed-line separation is 3.5mm, and the measured quality factor is shown in figure 4.8.

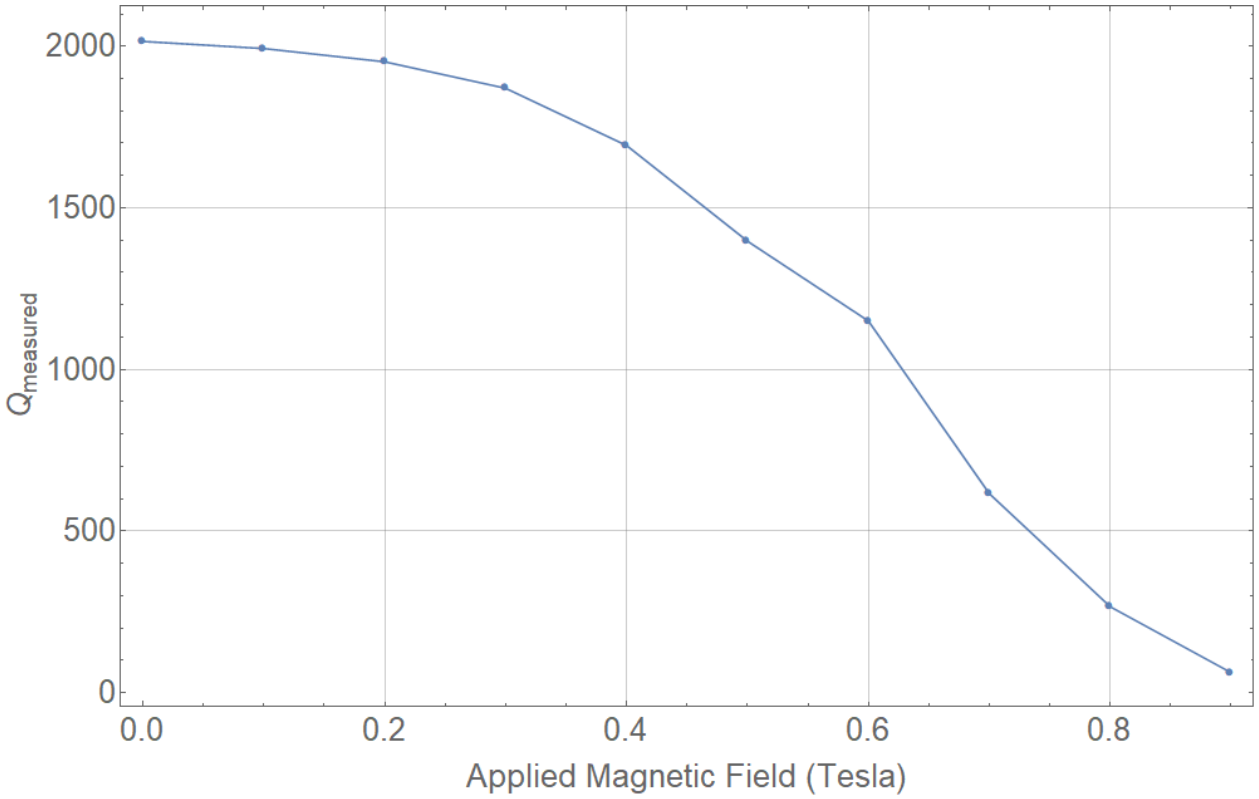

Figure 4.8: *The dependence of the quality factor, $Q_{measured}$, on the applied magnetic field strength, B.*

When no magnetic field is applied, the measured Q at 4 Kelvin is 2000. At a field of 0.1 T, a drop in Q to 1800 is observed. This drop increases further as the applied field moves to a maximum of 0.9 T where a Q of 200 is measured. The magnetic field dependent loss may be understood by two mechanisms: the creation and motion of vortices, or the generation of quasiparticles, within the superconducting film [14].

The microwave loss due to the motion of vorticies exists at higher magnetic field, as the superconducting film lives in a mixed state. The applied magnetic field can penetrate the film, interact with the current flowing in the vortices causing them to experience a torque. However, this loss may only be present due to the misalignment of the resonator to the parallel magnetic field. The induced motion of the vorticies requires work to be done, and

therefore introduces resistive loss in the resonator [22, 23, 24].

4.2.2 Aluminum Ball Bearing

In this experiment, an aluminum ball bearing, from McMaster Carr, is fixed within the birdcage. The object is to examine the existence of a magnetic field within the birdcage. The aluminum ball bearing measures 3mm in diameter and is made from weldable 2017 non-magnetic aluminum. A dielectric support is used to secure the ball bearing within the resonator. It is made from a rod of g10 fiberglass and measures 4mm in diameter. A 3 mm diameter semicircle, machined at the top of the rod, and 1.5mm deep is used to secure hold the ball bearing in the center of the resonator. Locite 409 is used to fix the ball bearing to the g10 rod.

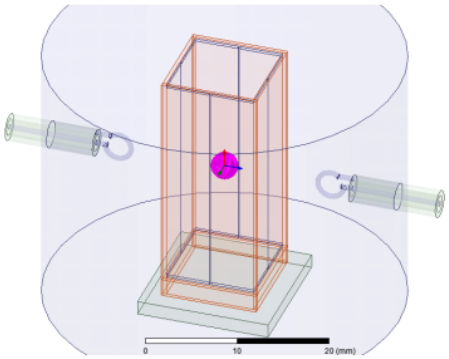

Figure 4.9: *Placement of the aluminum ball bearing in the center of the birdcage resonator. The aluminum ball bearing is 3mm in diameter. The center of the ball is aligned to the center of the package and the feed-line loops.*

4.2.2.1 Quality Factor

The experimental results, and measured Q values, are shown in figure 4.10 and table 4.3. Initially, the empty birdcage is measured again, followed by the g10 rod, and finally the g10 rod with the ball bearing.

The resonant frequency of the empty resonator is $f_0 = 3.219$ GHz. When the g10 rod is added, the resonant frequency is shifted slightly left to $f_0 = 3.21282$. A small drop in Q, from 4000 to 3900, is also observed due to the g10 dielectric material. The combination

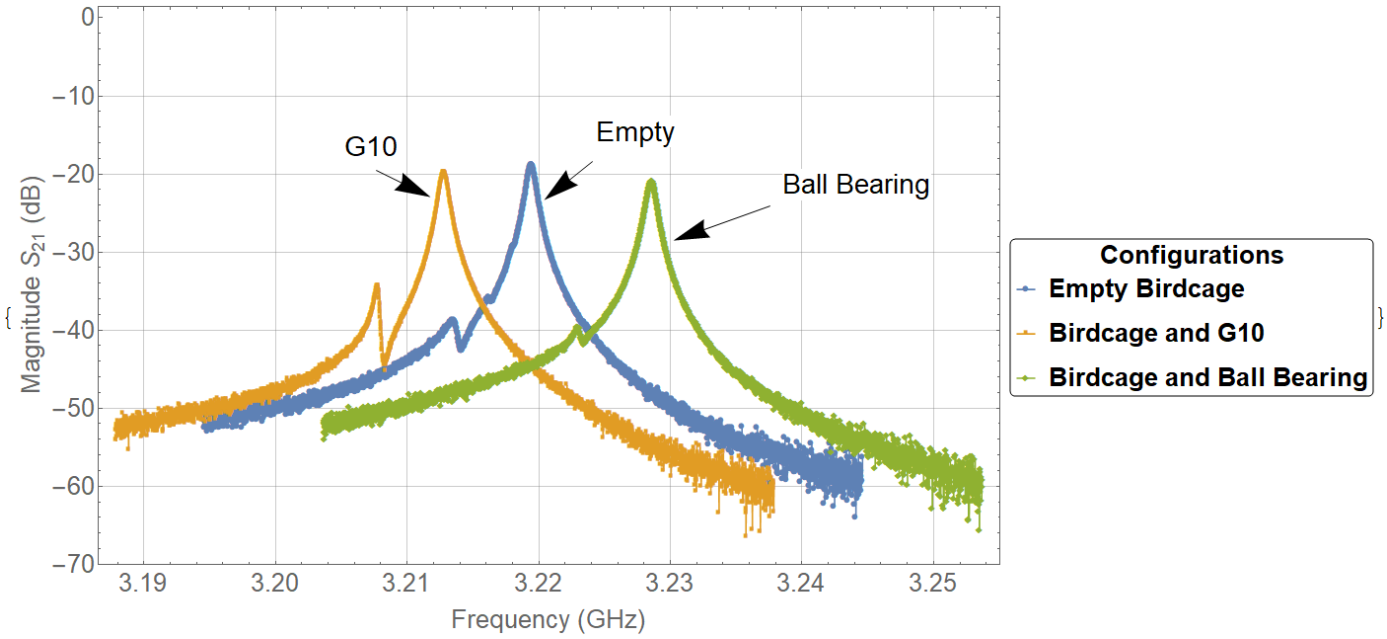

Figure 4.10: *Magnitude of S_{21} of the transverse mode of the empty resonator, the resonator with the dielectric support only, and the resonator with the dielectric support and aluminum ball bearing. The separation of the feed-line loops, to the resonator, is maintained at 6mm. A coupling between the feed-lines is still present as a peak adjacent to the resonance peak, at a lower frequency.*

of the g10 and the ball bearing, on the other hand, shifts the resonance frequency right to f_0= 3.228 GHz. The quality factor is further decreased from 4000 to 3750, due to the eddy current produced in the ball bearing. As in the case of the empty birdcage, the coupling between the feed-lines is still present as a peak at a lower frequency, adjacent to the resonance peak. However, in the case of the g10 rod within the resonator, it produces a much larger interaction than in the other experiments.

Configuration	Q	f_0 (GHz)	Loss (dB)
Empty Resonator	4000	3.21948	-18.7993
G10 Support	3900	3.21282	-19.8485
Ball Bearing and G10 Support	3750	3.22862	-20.9308

Table 4.3: *Measured values of Q, resonant frequency, and loss of the empty resonator, with the addition of the g10 rod, and the combination of the g10 rod and ball bearing.*

4.2.2.2 Simulated Current Distribution

A simulation of the current distribution along the surface of the aluminum ball bearing is shown in figure 4.11. As the magnetic flux interacts with the ball bearing it produces an

eddy current along its surface, perpendicular to the field. The surface current generates resistive loss in the birdcage, reducing the measured quality factor. The simulation is performed with an input power of 1 W, the measured Q is 5698, a slight drop from the empty resonator, and the resonance frequency is $f_0 = 3.0221$GHz. The power dissipated by the ball bearing is $P_{loss} = 0.032$W.

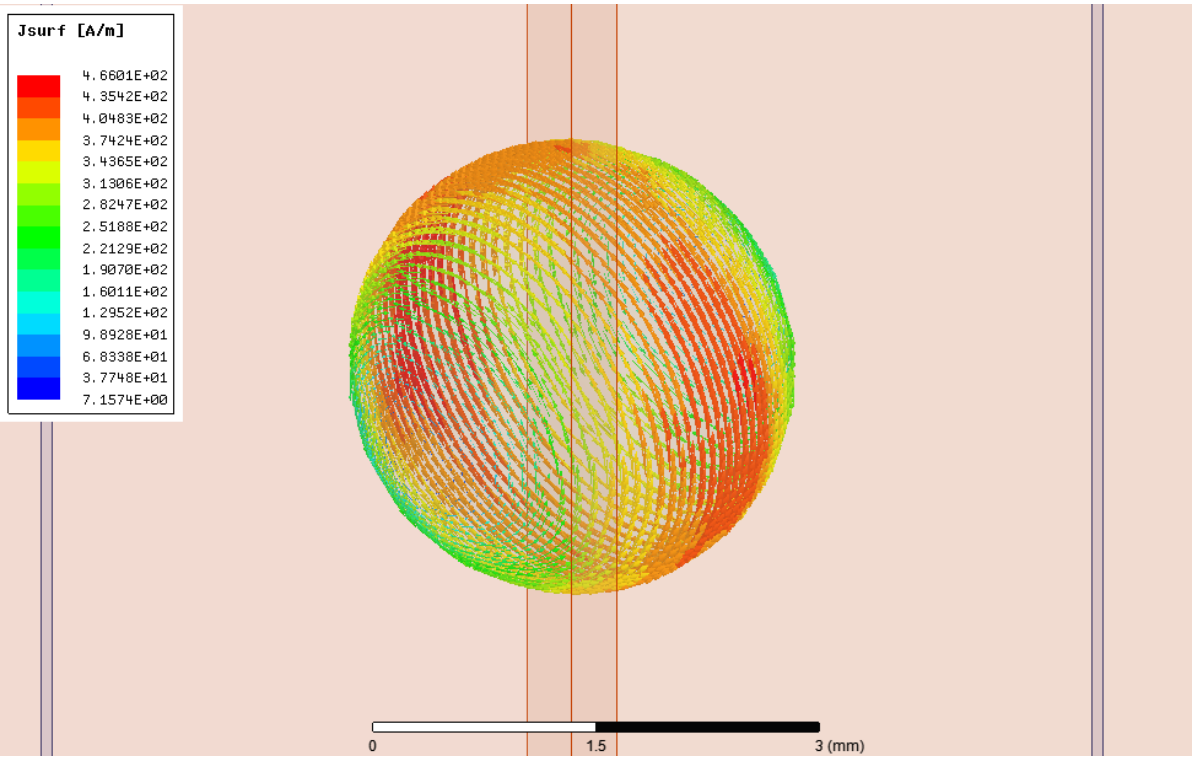

(a)

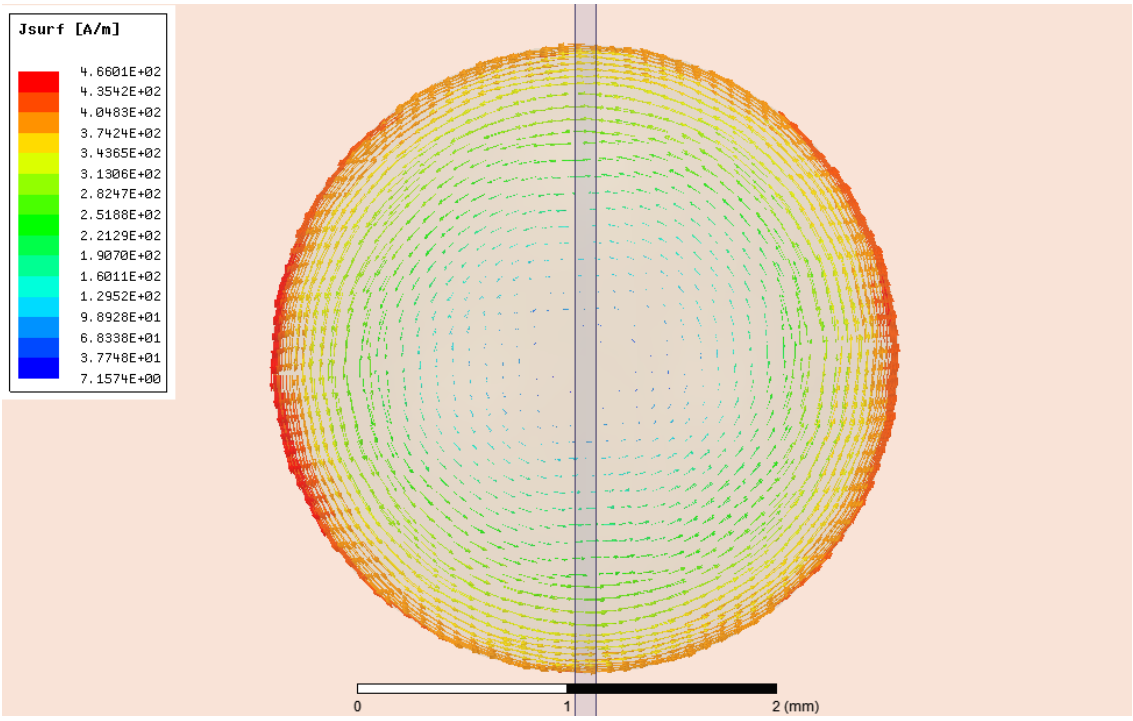

(b)

Figure 4.11: *Simulation of the surface current distribution of the birdcage resonator, with the addition of a aluminum ball bearing. The simulation is done using HFSS. The Q of the resonator is 5698, a drop of 100 from the Q of the empty resonator, and the resonance frequency is f_0 = 3.0221GHz, a shift of 0.0027 Ghz. The simulated input power, with the ball bearing, is P_{in} = 1 W, loss is P_{loss} = 0.032W, s_{21max} = -1.13dB.*

4.2.3 Aluminum Sheet

In this experiment, an aluminum sheet is placed within the center of birdcage. The object is to examine the orientation of the magnetic field within the birdcage. The sheet measures 15mm in length, 5 mm in width, and 0.3mm thick. A G10 rod is used to hold the sheet in place, and secured to the top of the copper package. The sheet are positioned in both possible orientations, with respect to the feed-lines, and their effects on the transverse magnetic field within the birdcage is observed. The first orientation is with the sheet edge aligned parallel to the feed-line loops, and in the second it is aligned perpendicular to the feed-lines. The two orientations are show in figure 4.12.

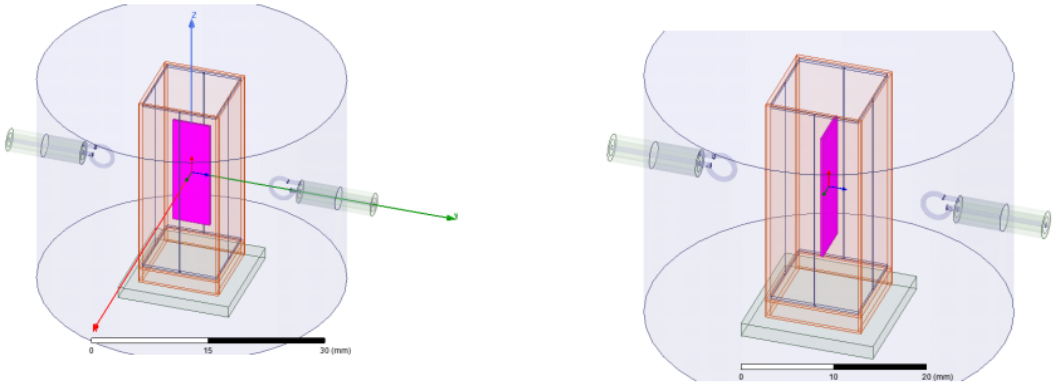

(a) **(b)**

Figure 4.12: *Placement of the aluminum sheet in two orientations within the resonator, where a) shows the parallel orientation and b) shows the perpendicular orientation. The aluminum sheet is 15mm in length, 5mm in width and 0.3mm in thickness. The center of the sheet is aligned to the center of the package and the feed-line loops.*

4.2.3.1 Quality Factor

The experimental results, and measured values of Q, are shown in figure 4.13 and table 4.4. With the aluminum sheet in the parallel orientation, as compared with the empty resonator, a drop in the measured Q to 3564 is observed. The resonant frequency is also shifted higher to $f_0 = 3.23022$ GHz. When the sheet is in the perpendicular orientation, both the measured Q and the resonant frequency, stay relatively the same to that of the empty resonator. The much larger surface area of the perpendicular sheet introduces less loss to the resonator than that of the parallel sheet. This result may be explained by the inverse relationship between the resistivity and the surface area of the conductor.

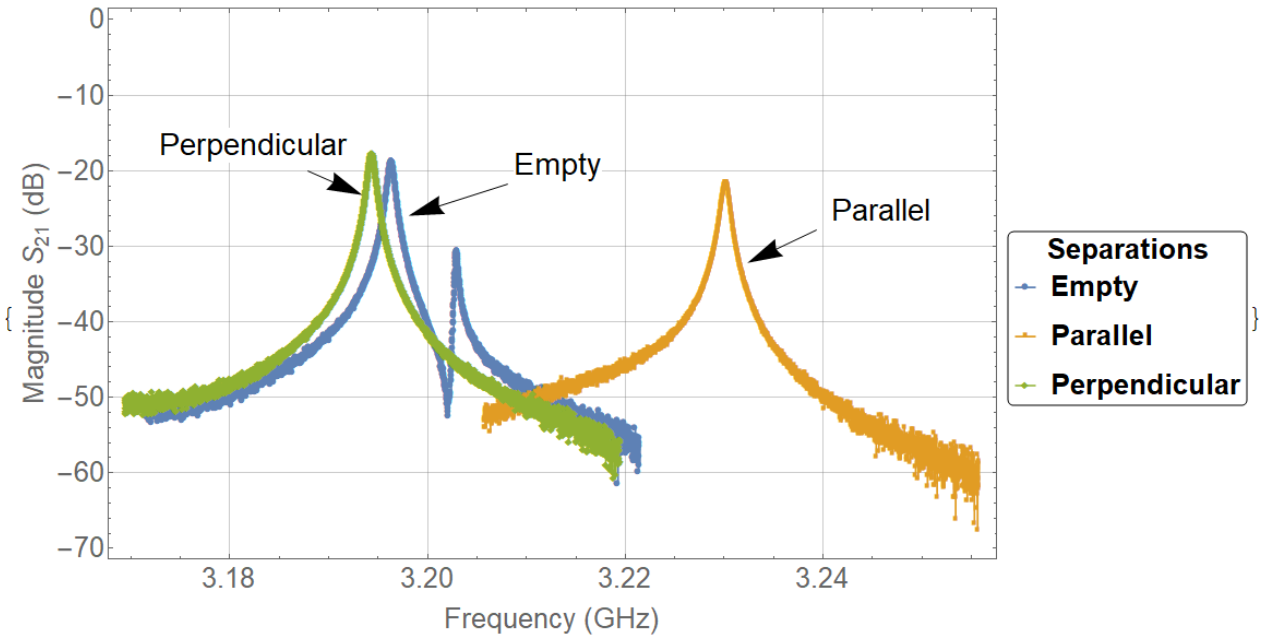

Figure 4.13: *Magnitude of S_{21} on the transverse mode of the empty resonator, the parallel, and the perpendicular orientation of an aluminum sheet inserted within the resonator. The feed-line separation is maintained at 6mm. The feed-line coupling is still present, as a peak to the right of the resonance peak of the empty resonator. However, with the presence of the aluminum sheet in different orientations, the coupling may be masked by the conductor.*

Configuration	Q	f_0 (GHz)	Loss (dB)
Empty Resonator	3934.06	3.19642	-17.7959
Sheet - Parallel	3564.35	3.23022	-21.642
Sheet - Perpendicular	3931.6	3.19442	-17.7959

Table 4.4: *Measured values of Q, resonant frequency f_0, and loss of the resonator with the addition of an aluminum sheet in multiple orientations.*

4.2.3.2 Simulated Current Distribution

In the parallel orientation, the surface current is distributed along the edge of the sheet. It is at a maximum at the edges, with a magnitude of 927.8 A/m, and decays towards the center. The quality factor is simulated to be $Q = 4377$, and the resonance frequency is $f_0 = 3.065$ GHz. This is a large relative drop in Q, when compared to the Q empty resonator of 5768. It is similar to that observed in the parallel experiment, where the smaller exposed conductive surface area may increase the resistivity of the resonator.

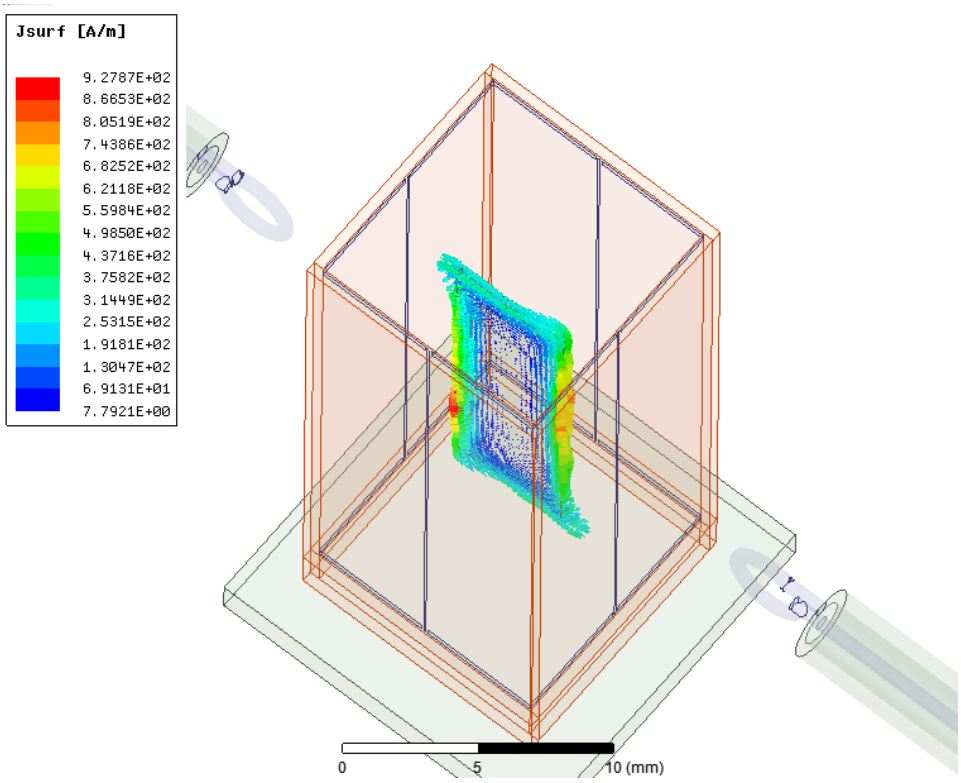

(a)

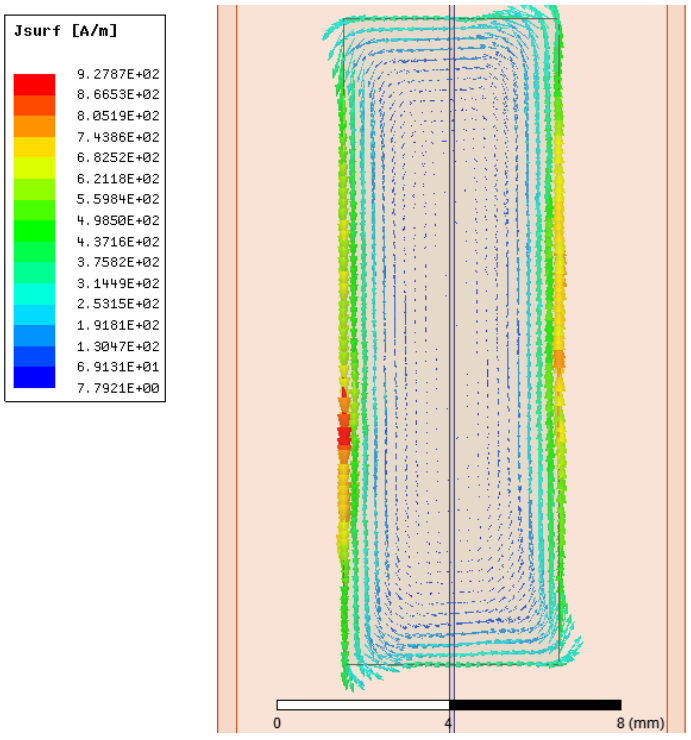

(b)

Figure 4.14: *Simulation of the current distribution in the aluminum sheet set in the parallel orientation. The input power, P_{in}, is set to 1W, the simulated loss is P_{loss} = 0.124 W, and the S_{21max} = -3.41dB. The simulated Q is 4377, a large drop in Q compared to the empty resonator, and f_0 = 3.06545, a shift of 0.046025GHz.*

In the perpendicular orientation, the surface current is distributed along the width of the sheet. It is maximized at the center, with a magnitude of 271.77 A/m, and decays towards the edge of the sheet. The quality factor is simulated to be $Q = 5036$, and the resonant frequency is $f_0 = 3.0216$GHz. The lower impact on both the quality factor and the resonant frequency, when compared with the empty resonator, may be explained by the larger surface area exposed to the electric field within the cavity. This result is similar to that observed in the perpendicular experiment.

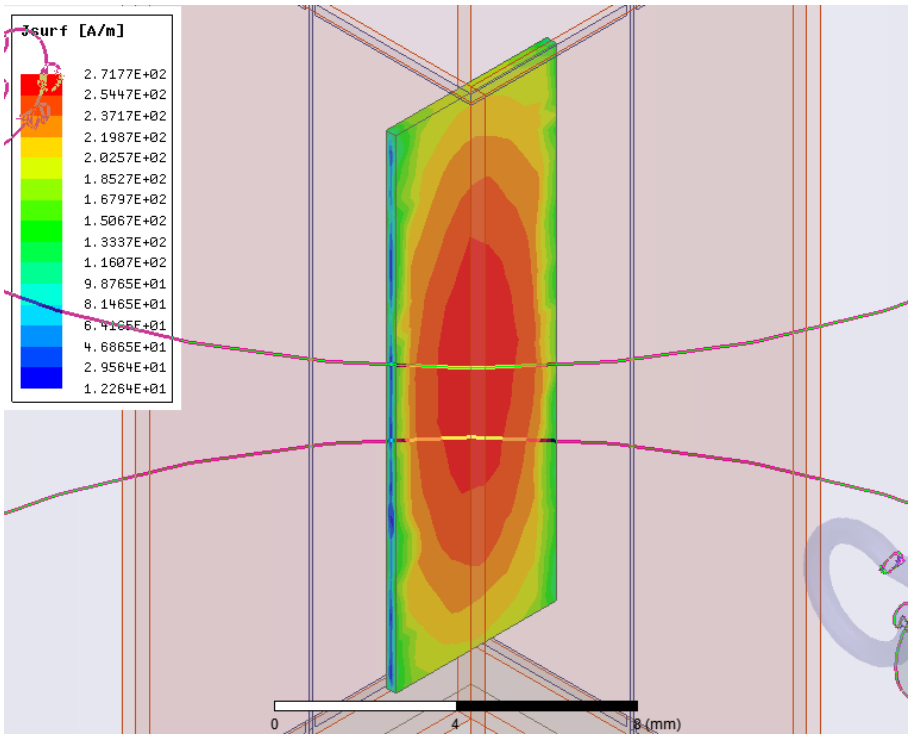

(a)

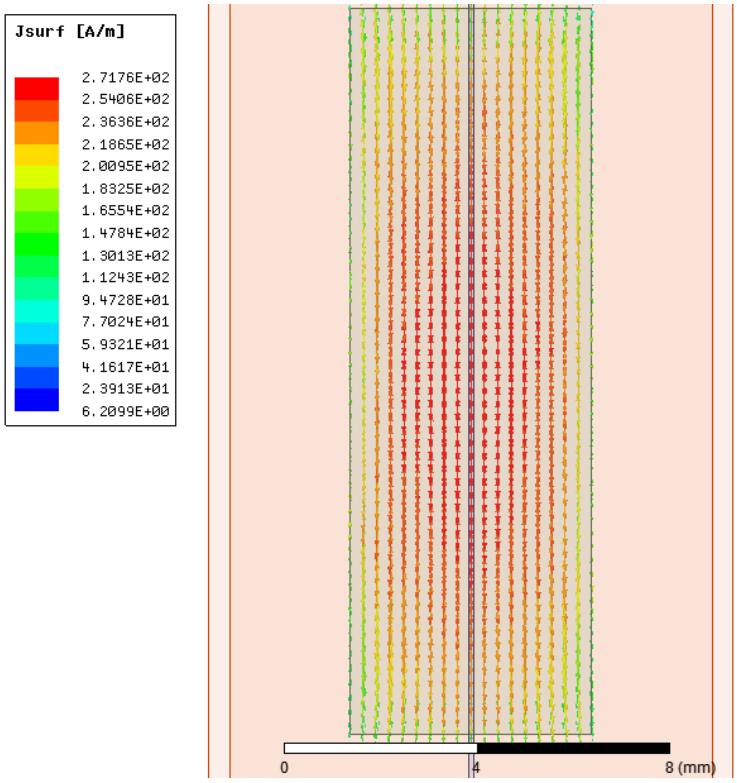

(b)

Figure 4.15: *Simulation of the surface current distribution with the aluminum sheet in the perpendicular orientation. The input power, P_{in}, is set to 1W, the simulated loss is P_{loss} = 0.094W, and the s_{21max} = -1.524dB. The simulated Q is 5036, a drop in Q of 732, and f_0 = 3.021675, a shift of 0.00225GHz.*

Chapter 5

Conclusion

5.1 Conclusion

The analysis, fabrication, and characterization of superconductor microwave resonators as the building blocks of a birdcage coil for NMR has been presented.

The circuit analysis, presented in section 4.1, was based on a lumped-element eigenanalysis of the ladder network modeling the resonators. It was used to derive the operating frequency of the transverse mode of an idealized birdcage resonator. A perturbation parameter was latter added in order to describe the effects that potential misalignment in the construction of the coil. The misalignment was modeled as a gap between the ring element of two adjacent resonator faces. Increasing the perturbation lead to an increase of 0.4 GHz in the transverse mode.s Simulations of the field distribution and surface currents in the coil, in various experimental conditions presented in section 4.2, were also conducted. These simulations describe the dynamics of the circularly polarized field, as well as power loss in the coil.

The fabrication, and latter assembly, of the birdcage coil was conducting in the Omicron UHV and Quantum Nanofabrication laboratory. The superconducting resonators, which make up the birdcage coil, were fabricated from superconducting niobium films and sapphire substrates. The quality factor of the birdcage coil was characterized in a low temperature environment.

The characterization of the birdcage resonator, presented in section 4.2, shows a modest improvement in Q, up to 4000, compared to room temperature system which may have a Q of only a few hundred [25]. This improvement is based on the use of superconducting niobium films. In section 4.2.1, the feed-line separation, power dependence, and magnetic field dependence of the empty resonator was measured. We learned that by increasing the separation between the external circuitry from the surface of the resonator, from 4mm to 6mm,

we were able to improve the measured Q of the resonator from 3450 to 4000. The diameter of the copper packaging, used to house the resonator in low temperature experiments, can be further expanded to increase the measured Q, by reducing the effects of the coupling Q of the external circuit. The power dependent measurement of the resonator showed an increase of the kinetic inductance and a resonant frequency shift to lower frequencies. This is a result of a change in the current distribution at higher input microwave powers. From the magnetic field dependence measurement, the superconducting state of the resonator degrades as we increased the applied magnetic fields. This is reflected in the drop in Q from 2000 at 0 T field to 200 at 0.8 T, as the resonator becomes more lossy.

In section 4.2.2, an aluminum ball bearing was added within the resonator, supported by a machined g10 rod. In simulations, the magnetic field created within the empty resonator is perturbed by the ball bearing. This suggests the induced surface current in the ball bearing acts as a new source of loss in the resonator, decreasing the Q. From the results, a small loss of Q, from 5780 to 5698, and a resonant frequency shift, from 3.0200 to 3.0221 GHZ, was observed. In the experimental measurement, we were able to confirm the existence of this magnetic field by measuring the drop in Q of the resonator, as compared with the empty resonator. We measured a decrease in Q from 4000 to 3750 and an increase in resonance frequency from 3.219 to 3.229 GHz.

In section 4.2.3, an aluminum sheet was added within the resonator, suspended by a g10 support rod. The orientation of the aluminum sheet, with respect to the feed-line loops, was modified in order to detect the direction of the magnetic field produced by the birdcage resonator. When the aluminum sheet is oriented perpendicular to the feed-line loops, we measured a small drop in Q, from 3934 to 3931, and a loss of -17.79dB. When the sheet is oriented parallel to the loops, a larger drop in Q, to 3564 and loss of -21.64dB is measured. This experimentally confirms that the magnetic field is oriented perpendicular to the feed-line loops, as the small conductive surface area in the direction of the electric field interferes greatest with the measured Q and loss of the resonator. This orientation generates both larger surface currents, on the sheet, as well as a higher power loss in the resonator.

In conclusion, in the analysis and characterization of the birdcage resonator, we learned about the important impact assembly of 2D planar resonator into a 3D birdcage has on the frequency modes, that modest values of Q are attainable and can be further improved by reducing the coupling Q. The aluminum ball bearing demonstrated that the birdcage resonator was able to create a magnetic field within the resonator, and we were able to confirm the relative orientation with respect to the feed-line excitation. However, only a modest value of Q, as well as the loss due external magnetic field, and applied power levels leaves room for improvement in the design of the superconducting birdcage resonator.

Bibliography

[1] Zhi-Pei Liang and Paul C Lauterbur. *Principles of magnetic resonance imaging: a signal processing perspective*. SPIE Optical Engineering Press, 2000.

[2] Peter Hugo Sprenger. *Birdcage resonator design in magnetic resonance imaging*. PhD thesis, Massachusetts Institute of Technology, 1995.

[3] Yonatan Abebe Tadesse. *The Electromagnetic Simulation of Birdcage Coils for MRI based on Finite Element Method*. PhD thesis, Youngstown State University, 2016.

[4] David M Pozar. Microwave engineering 3e. *Tramsmission Lines and Waveguides*, pages 143–149, 2005.

[5] Mike J Lancaster. *Passive microwave device applications of high-temperature superconductors*. Cambridge University Press, 2006.

[6] Hamidreza Mohebbi, David G Cory, and Grum Teklemariam. Birdcage resonator for magnetic resonance, February 23 2017. US Patent App. 15/307,088.

[7] Mathieu Sarracanie, Cristen D LaPierre, Najat Salameh, David EJ Waddington, Thomas Witzel, and Matthew S Rosen. Low-cost high-performance mri. *Scientific reports*, 5:15177, 2015.

[8] RD Black, PB Roemer, A Mogro-Campero, LG Turner, and KW Rohling. High temperature superconducting resonator for use in nuclear magnetic resonance microscopy. *Applied physics letters*, 62(7):771–773, 1993.

[9] Chang-Beom Eom and James M Murduck. Synthesis and characterization of superconducting thin films. In *Thin Films*, volume 28, pages 227–270. Elsevier, 2001.

[10] AF Mayadas, RB Laibowitz, and JJ Cuomo. Electrical characteristics of rf-sputtered single-crystal niobium films. *Journal of Applied Physics*, 43(3):1287–1289, 1972.

[11] AR Wildes, J Mayer, and K Theis-Bröhl. The growth and structure of epitaxial niobium on sapphire. *Thin solid films*, 401(1-2):7–34, 2001.

[12] Jean-Claude Villegier, S Bouat, P Cavalier, R Setzu, R Espiau de Lamaestre, Corentin Jorel, Philippe Odier, Bruno Guillet, Laurence Méchin, Marie-Pierre Chauvat, et al. Epitaxial growth of sputtered ultra-thin nbn layers and junctions on sapphire. *IEEE Transactions on Applied Superconductivity*, 19(3):3375–3378, 2009.

[13] Adam N McCaughan. High-q superconducting coplanar waveguide resonators for integration into molecule ion traps. Technical report, Massachusetts institute of technology department of electrical engineering and computer science, 2010.

[14] Sangil Kwon, Anita Fadavi Roudsari, Olaf WB Benningshof, Yong-Chao Tang, Hamid R Mohebbi, Ivar AJ Taminiau, Deler Langenberg, Shinyoung Lee, George Nichols, David G Cory, et al. Magnetic field dependent microwave losses in superconducting niobium microstrip resonators. *arXiv preprint arXiv:1802.05183*, 2018.

[15] Cecil E Hayes, William A Edelstein, John F Schenck, Otward M Mueller, and Matthew Eash. An efficient, highly homogeneous radiofrequency coil for whole-body nmr imaging at 1.5 t. *Journal of Magnetic Resonance (1969)*, 63(3):622–628, 1985.

[16] G.H Glover, C.E Hayes, N.J Pelc, W.A Edelstein, O.M Mueller, H.R Hart, C.J Hardy, M O'Donnell, and W.D Barber. Comparison of linear and circular polarization for magnetic resonance imaging. *Journal of Magnetic Resonance (1969)*, 64(2):255–270, 1985.

[17] Mark C. Leifer. Resonant modes of the birdcage coil. *Journal of Magnetic Resonance*, 124(1):51–60, 1997.

[18] James Tropp. The theory of the bird-cage resonator. *Journal of Magnetic Resonance (1969)*, 82(1):51–62, 1989.

[19] GEH Reuter and EH Sondheimer. The theory of the anomalous skin effect in metals. *Proc. R. Soc. Lond. A*, 195(1042):336–364, 1948.

[20] C Clavero, DB Beringer, WM Roach, JR Skuza, KC Wong, AD Batchelor, CE Reece, and RA Lukaszew. Strain effects on the crystal growth and superconducting properties of epitaxial niobium ultrathin films. *Crystal Growth & Design*, 12(5):2588–2593, 2012.

[21] Michael D. Harpen. Equivalent circuit for birdcage resonators. *Magnetic Resonance in Medicine*, 29(2):263–268, 1993.

[22] HR Mohebbi, OWB Benningshof, IAJ Taminiau, GX Miao, and DG Cory. Composite arrays of superconducting microstrip line resonators. *Journal of Applied Physics*, 115(9):094502, 2014.

[23] Chunhua Song, Michael P DeFeo, Kang Yu, and Britton LT Plourde. Reducing microwave loss in superconducting resonators due to trapped vortices. *Applied Physics Letters*, 95(23):232501, 2009.

[24] D Bothner, C Clauss, E Koroknay, M Kemmler, T Gaber, M Jetter, M Scheffler, P Michler, M Dressel, D Koelle, et al. Reducing vortex losses in superconducting microwave resonators with microsphere patterned antidot arrays. *Applied Physics Letters*, 100(1):012601, 2012.

[25] J. Thomas Vaughan and John R Griffiths. *RF coils for MRI*. John Wiley and Sons Ltd., 2012.

[26] Ray Freeman. *Magnetic resonance in chemistry and medicine*. Oxford University Press on Demand, 2003.

[27] Michael Tinkham. *Introduction to superconductivity*. Courier Corporation, 2004.

[28] Paul Seidel. *Applied Superconductivity: Handbook on Devices and Applications*. John Wiley & Sons, 2015.

[29] C Jo Gorter and HBG Casimir. The thermodynamics of the superconducting state. *Z. tech. Phys*, 15:539–42, 1934.

[30] Egor Kiselev. Design and measurement of superconducting spiral microwave resonators entwurf und vermessung supraleitender.

[31] RH Parmenter. Rh parmenter, rca rev. 23, 323 (1962). *RCA Rev.*, 23:323, 1962.

[32] J Gittleman, B Rosenblum, TE Seidel, and AW Wicklund. Nonlinear reactance of superconducting films. *Physical Review*, 137(2A):A527, 1965.

[33] M.C. Lin, Ch. Wang, L.H. Chang, G.H. Luo, and M.K. Yeh. Effects of material properties on resonance frequency of a cesr-iii type 500 mhz srf cavity. *Proceedings of the 2003 Bipolar/BiCMOS Circuits and Technology Meeting (IEEE Cat. No.03CH37440)*.

[34] Kiyotaka Wasa, Makoto Kitabatake, and Hideaki Adachi. *Thin films material technology*. William Andrew, 2004.

[35] J. Wosik, Lei-Ming Xie, K. Nesteruk, Lian Xue, J.A. Bankson, and J.D. Hazle. Superconducting single and phased-array probes for clinical and research mri. *IEEE Transactions on Appiled Superconductivity*, 13(2):1050–1055, 2003.

[36] Q D Jiang, Y L Xie, W B Zhang, H Gu, Z Y Ye, K Wu, J L Zhang, C Y Li, and D L Yin. Superconductivity and transport properties in ultrathin epitaxial single-crystal niobium films. *Journal of Physics: Condensed Matter*, 2(15):3567, 1990.

[37] M. A. Golosovsky, H. J. Snortland, and M. R. Beasley. Nonlinear microwave properties of superconducting nb microstrip resonators. *Physical Review B*, 51(10):6462–6469, 1995.

[38] A. I. Gubin, K. S. Il'in, S. A. Vitusevich, M. Siegel, and N. Klein. Dependence of magnetic penetration depth on the thickness of superconducting nb thin films. *Phys. Rev. B*, 72:064503, Aug 2005.

[39] Giulio Giovannetti. Birdcage coils: Equivalent capacitance and equivalent inductance. *Concepts in Magnetic Resonance Part B: Magnetic Resonance Engineering*, 44(2):32–38, 2014.

[40] Giulio Giovannetti, Vittorio Viti, Yongjun Liu, Wenhua Yu, Raj Mittra, Luigi Landini, and Antonio Benassi. An accurate simulator for magnetic resonance coil sensitivity estimation. *Concepts in Magnetic Resonance Part B: Magnetic Resonance Engineering: An Educational Journal*, 33(4):209–215, 2008.

[41] Thomas KF Foo, Cecil E Hayes, and Yoon-Won Kang. An analytical model for the design of rf resonators for mr body imaging. *Magnetic resonance in medicine*, 21(2):165–177, 1991.

[42] Kenneth W Fishbein, Joseph C McGowan, and Richard G Spencer. Hardware for magnetic resonance imaging. In *MR Imaging in White Matter Diseases of the Brain and Spinal Cord*, pages 13–28. Springer, 2005.

[43] F David Doty, George Entzminger Jr, Cory D Hauck, and John P Staab. Practical aspects of birdcage coils. *Journal of magnetic resonance (San Diego, Calif.: 1997)*, 138(1):144–154, 1999.

[44] Thomas Vullo, Raymond T Zipagan, Romeo Pascone, Joseph P Whalen, and Patrick T Cahill. Experimental design and fabrication of birdcage resonators for magnetic resonance imaging. *Magnetic resonance in medicine*, 24(2):243–252, 1992.

[45] Chunsheng Wang and Gary X Shen. B1 field, sar, and snr comparisons for birdcage, tem, and microstrip coils at 7t. *Journal of Magnetic Resonance Imaging: An Official Journal of the International Society for Magnetic Resonance in Medicine*, 24(2):439–443, 2006.

[46] David I Hoult and RE Richards. The signal-to-noise ratio of the nuclear magnetic resonance experiment. *Journal of Magnetic Resonance (1969)*, 24(1):71–85, 1976.

[47] Giulio Giovannetti, Raffaello Francesconi, Luigi Landini, Maria Filomena Santarelli, Vincenzo Positano, Vittorio Viti, and Antonio Benassi. Conductor geometry and capacitor quality for performance optimization of low-frequency birdcage coils. *Concepts in Magnetic Resonance Part B: Magnetic Resonance Engineering: An Educational Journal*, 20(1):9–16, 2004.

[48] Michael D Harpen. Radiative losses of a birdcage resonator. *Magnetic resonance in medicine*, 29(5):713–716, 1993.

[49] Srinivasan Kathiravan and Jagannathan Kanakaraj. A review on potential issues and challenges in mr imaging. *The Scientific World Journal*, 2013, 2013.

[50] DI Hoult. The principle of reciprocity in signal strength calculations—a mathematical guide. *Concepts in Magnetic Resonance: An Educational Journal*, 12(4):173–187, 2000.

[51] QY Ma, KC Chan, Daniel F Kacher, Erzhen Gao, Mei Sim Chow, Kelvin K Wong, Hui Xu, Edward S Yang, Geoff S Young, Jason R Miller, et al. Superconducting rf coils for clinical mr imaging at low field1. *Academic radiology*, 10(9):978–987, 2003.

[52] P Styles, NF Soffe, CA Scott, DA Crag, F Row, DJ White, and PCJ White. A high-resolution nmr probe in which the coil and preamplifier are cooled with liquid helium. *Journal of Magnetic Resonance (1969)*, 60(3):397–404, 1984.

[53] QY Ma. Rf applications of high temperature superconductors in mhz range. *IEEE transactions on applied superconductivity*, 9(2):3565–3568, 1999.

[54] John C Nouls, Michael G Izenson, Harold P Greeley, and G Allan Johnson. Design of a superconducting volume coil for magnetic resonance microscopy of the mouse brain. *Journal of magnetic resonance*, 191(2):231–238, 2008.

[55] AS Hall, N McN Alford, TW Button, DJ Gilderdale, KA Gehring, and IR Young. Use of high temperature superconductor in a receiver coil for magnetic resonance imaging. *Magnetic resonance in medicine*, 20(2):340–343, 1991.

[56] L Darrasse and J-C Ginefri. Perspectives with cryogenic rf probes in biomedical mri. *Biochimie*, 85(9):915–937, 2003.

[57] Hsu-Lei Lee, In-Tsang Lin, Jyh-Horng Chen, Herng-Er Horng, and Hong-Chang Yang. High-t/sub c/superconducting receiving coils for nuclear magnetic resonance imaging. *IEEE transactions on applied superconductivity*, 15(2):1326–1329, 2005.

[58] William H Hartwig. Superconducting resonators and devices. *Proceedings of the IEEE*, 61(1):58–70, 1973.

[59] BR McAvoy, GR Wagner, JD Adam, J Talvacchio, and M Driscoll. Superconducting stripline resonator performance. *IEEE Transactions on Magnetics*, 25(2):1104–1106, 1989.

[60] Salvador H Talisa, Michael A Janocko, Charles Moskowitz, J Talvacchio, JF Billing, R Brown, DC Buck, CK Jones, BR McAvoy, GR Wagner, et al. Low-and high-temperature superconducting microwave filters. *IEEE transactions on microwave theory and techniques*, 39(9):1448–1454, 1991.

[61] MJ Lancaster, TSM Maclean, Z Wu, A Porch, P Woodall, and N NcN Alford. Superconducting microwave resonators. In *IEE Proceedings H (Microwaves, Antennas and Propagation)*, volume 139, pages 149–156. IET, 1992.

[62] RS Withers, G-C Liang, BF Cole, and M Johansson. Thin-film hts probe coils for magnetic-resonance imaging. *IEEE transactions on applied superconductivity*, 3(1):2450–2453, 1993.

[63] Orest G Vendik, Irina B Vendik, and Tatyana B Samoilova. Nonlinearity of superconducting transmission line and microstrip resonator. *IEEE transactions on microwave theory and techniques*, 45(2):173–178, 1997.

[64] JM Hornibrook, EE Mitchell, CJ Lewis, and DJ Reilly. Parasitic losses in nb superconducting resonators. *Physics Procedia*, 36:187–192, 2012.

[65] Jerzy Krupka, Krzysztof Derzakowski, Michael Tobar, John Hartnett, and Richard G Geyer. Complex permittivity of some ultralow loss dielectric crystals at cryogenic temperatures. *Measurement Science and Technology*, 10(5):387, 1999.

[66] MC Lin, Ch Wang, LH Chang, GH Luo, and MK Yeh. Effects of material properties on resonance frequency of a cesr-iii type 500 mhz srf cavity. In *Particle Accelerator Conference, 2003. PAC 2003. Proceedings of the*, volume 2, pages 1371–1373. IEEE, 2003.

[67] Sormeh Setoodeh. Superconducting microwave filters. Master's thesis, University of Waterloo, 2011.

[68] Thijs Boehme. Characterisation and optimisation of superconducting microwave resonators.

[69] Marta Krawczyk. Microstrip resonators for circuit quantum electrodynamics. 2011.

[70] Monica MC Allain and Brent J Heuser. Lattice strain measurements of deuteride (hydride) formation in epitaxial nb: Additional results and further insights into past measurements. *Physical Review B*, 72(5):054102, 2005.

[71] Oleksandr V Dobrovolskiy and Michael Huth. Crossover from dirty to clean superconducting limit in dc magnetron-sputtered thin nb films. *Thin Solid Films*, 520(18):5985–5990, 2012.

[72] K Il'in, D Rall, M Siegel, A Engel, A Schilling, A Semenov, and H-W Huebers. Influence of thickness, width and temperature on critical current density of nb thin film structures. *Physica C: Superconductivity*, 470(19):953–956, 2010.

[73] Dragan Janjušević, Mihael Sran Grbić, Miroslav Požek, Antonije Dulčić, Dalibor Paar, Bernd Nebendahl, and Thomas Wagner. Microwave response of thin niobium films under perpendicular static magnetic fields. *Physical Review B*, 74(10):104501, 2006.

[74] Jeremy M Sage, Vladimir Bolkhovsky, William D Oliver, Benjamin Turek, and Paul B Welander. Study of loss in superconducting coplanar waveguide resonators. *Journal of Applied Physics*, 109(6):063915, 2011.

[75] QD Jiang, YL Xie, WB Zhang, H Gu, ZY Ye, K Wu, JL Zhang, CY Li, and DL Yin. Superconductivity and transport properties in ultrathin epitaxial single-crystal niobium films. *Journal of Physics: Condensed Matter*, 2(15):3567, 1990.

[76] YiRong Jin, XiaoHui Song, and DianLin Zhang. Grain-size dependence of superconductivity in dc sputtered nb films. *Science in China Series G: Physics, Mechanics and Astronomy*, 52(9):1289–1292, 2009.

[77] R Banerjee, EA Sperling, GB Thompson, HL Fraser, S Bose, and P Ayyub. Lattice expansion in nanocrystalline niobium thin films. *Applied physics letters*, 82(24):4250–4252, 2003.